Energy & Materials Transition
www.tno.nl
+31 88 866 42 56
info@tno.nl

TNO2023_R11303

TNO2023_R11303 – 16 November 2023

SRIMA: Background Information of the Python tool

Author(s)	Fokker, P.A., Buijze, L., Pluymaekers, M.P.D.
Classification report	TNO Public
Title	
Number of pages	60
Number of appendices	0

Contents

Abstract

This report describes the technical background of the SRIMA tool (Seal and Reservoir Integrity through Mechanical Analysis). The SRIMA tool is used in the Standard extended Seismic Hazard Analysis (Standaard uitgebreide SDRA), which is part of the seismic hazard and risk assessment for geothermal projects in the Netherlands (Mijnlieff et al., 2023). SRIMA is a fast semi-analytical tool that provides a scenario-based analysis of pressure and temperature changes around an injection well, the resulting stress changes on nearby faults, reactivated fault area, the maximum credible earthquake magnitude, the resulting PGV distribution and an estimate of damage. SRIMA also computes the potential for development of tensile fracture in the seal and base. SRIMA is designed to give first-order estimates of these results. All calculations can be performed in a stochastic framework, which allows the assessment of failure probabilities.

SRIMA is based on semi-analytical expressions for the fast calculation of temperatures, pressures, and induced poro-elastic and thermo-elastic stresses due to the injection of cold fluid. The expressions for flow and induced stresses have been developed for a homogeneous, isotropic layer cake model under radial symmetry. In the injection layer the flow is assumed to be fully developed and temperature transfer is in an advective way. In the bounding seal and base layers, the pressure and temperature dynamics are assumed diffusive. The derived expressions capture the first-order characteristics of the pressure, temperature and stress changes. Validation of the expressions has been achieved through comparison with finite-difference and finite-element codes for temperature, pressure, and stress changes around an injection well. A fault without offset cutting through the seal, reservoir, and base can be specified within the model space. Poro-elastic and thermo-elastic stress changes are transformed to fault stresses and fault criticality. The fault area over which stresses are critical (i.e. fault reactivation occurs) is used to estimate the magnitude of the largest credible earthquake for each model scenario, assuming that the entire reactivated fault area participates in a single event, slip cannot propagate beyond the reactivated area, and all assumed slip over the fault area is seismic slip. An ensemble of magnitudes is converted to exceedance curves of peak ground velocities (PGV) by using the GMPE of Ruigrok & Dost (2021). The resulting PGV distribution serves as input for calculating the probability of exceeding Damage State 1 using the empirical fragility functions of Crowley et al. (2019) for unreinforced masonry buildings. In this report the details and assumptions behind each step are summarized.

1 Introduction

The majority of geothermal operations in the Netherlands target porous sandstone formations at 2-3 km deep – so-called matrix-type geothermal reservoirs (Mijnlieff, 2020). Heat is extracted from these formations by pumping up hot pore water through a production well, extracting the heat at the surface through a heat exchanger, and reinjecting the cold water into an injection well in the same formation, achieving a balanced circulation. The injection of fluids and extraction of heat alters the state of stress in the subsurface, and may lead to fracturing or fault reactivation. For each geothermal production license, the Mining Law requires an estimate of the ground motions and risk to the local population: a Seismic Hazard and Risk Analysis (Mijnlieff et al., 2023). Furthermore, the safety of geothermal operations in matrix-type geothermal reservoirs requires that circulated water remains in the target aquifer to which it was injected. This implies that the integrity of the seal, overburden and underburden must be safeguarded. Hydraulic fracturing is a phenomenon that can breach this integrity, as it can break intact formation and create a conductive flow path through the seal. Therefore, it is important to quantitatively assess both effects of geothermal operations on the (sub)surface.

Both hydraulic fracturing and fault reactivation depend directly on the stresses and the pore pressures. The assessment of the risk of integrity issues therefore requires knowledge of the pressure and stress development in the reservoir, the seal, and the base. For geothermal operations, the largest stress changes in the reservoir and in adjacent layers are related to the injection of relatively cold water (Buijze et al., 2021, Kivi et al., 2022, Hutka et al., 2023). Two main phenomena must be incorporated if the stress development is to be assessed. In the first place, injection of water is associated with elevated pore pressures, and in the second place, injection of water is associated with cooling of the rock around the injection well. Subsurface properties are however associated with a large degree of uncertainty. Therefore, there is a need for calculation methods that allow for probabilistic, scenario-based assessments, with the incorporation of ranges of the input parameters to capture uncertainties in these parameters. Such tools also need to be fast and flexible, and they are provided by analytical or semi-analytical means.

One of the available methods is the tool SRIMA, an acronym for Seal and Reservoir Integrity through Mechanical Analysis (Buijze et al., 2021, Fokker et al., 2023). SRIMA is a fast, semi-analytical tool that gives a first-order computation of the temperature, pressure and stress changes around a geothermal injection well. The effective stresses are used to assess the possibility of tensile stress creation and hydraulic fracturing, and of shear failure that can lead to induced seismicity.

The document at hand describes the model choices underlying the updated SRIMA tool (version 1.0.3), the semi-analytical expressions that it is based on, and the results of validation exercises. This version of SRIMA is used in the Standard extended Seismic Hazard Analysis (Standaard uitgebreide SDRA), which is part of the seismic hazard and risk assessment for geothermal projects in the Netherlands (Mijnlieff et al., 2023). With respect to the earlier documents on SRIMA (Buijze et al., 2021, Fokker et al. 2023), the implementation described here is extended further in the direction of actual risks. A basic assessment of hydraulic fracturing risk upon tensile failure has been added, including the possibility to assess the deployment of maximum injection rates larger than the average injection rate. A first-order

assessment of the hydraulic fracture growth or the reactivated area of a fault within the cooled volume is provided. In order to use SRIMA within the Seismic Hazard and Risk Analysis framework, the magnitude of the largest credible earthquake is computed, based on reactivated fault area, and the associated peak ground velocities and damage.

2 Model choices and Mathematical Formulation

SRIMA is a semi-analytical tool that helps the user perform quick mechanical calculations to assess the possibility of fault reactivation and hydraulic fracturing. If fault reactivation is possible, it also assesses the magnitude of the largest credible earthquake and the associated peak ground velocity. It furthermore supports stochastic analyses to assess the effect of parameter uncertainty. The requirements of calculation speed and the possibility of stochastic calculations form the background of many model choices in SRIMA.

2.1 Model geometry, pressure, and temperature

2.1.1 Basic assumptions

The tool has been developed for a radially-symmetric reservoir where fluid is injected in a well in its center (Figure 1). Three layers are present: the permeable layer in which the injection takes place, and the overlying and underlying, low-permeability layers. Therefore, pressure and temperature fields are also radially symmetric. Injection is modelled as taking place evenly over the complete height of the aquifer. Pressure and temperature fields are assumed to be independent of the vertical position in the aquifer. In the aquifer, flow is modelled under steady-state conditions and heat transport is assumed to take place by advection only. In the bounding layers both pressure and temperature are assumed to be controlled by diffusion (Carslaw & Jaeger, 1992; Dake, 1983; Nield & Bejan, 2006). These model choices facilitate the use of analytical expressions for pressure, temperature and stress (Candela, Van der Veer, & Fokker, 2018; Myklestad, 1942; Perkins & Gonzalez, 1985). A (virtual) fault can be defined as a plane at any position and orientation, as long as it is a no-flow barrier and does not introduce an offset between reservoir parts (see Section A.1.3 on the effect of offset on induced stress changes).

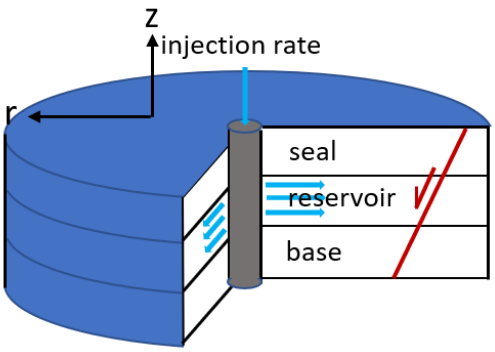

Figure 1 Radially-symmetric geometry used in SRIMA for analysis of thermo- and poro-elastic stresses in a reservoir caused by injection of cold fluids. Injection is assumed to take place over the entire reservoir height.

The radial symmetry comes with limitations. First, anisotropy of the permeability or effects of a production well cannot be incorporated. Consequently, also the temperature profile is radially symmetric, but this still catches the main effect of cooling and pressurization around the reservoir. The induced stresses, although also radially symmetric, do not preclude anisotropy: a virgin stress field that is anisotropic with different values for the minimum and maximum horizontal stress can be incorporated as background field. In addition, in SRIMA it is assumed the fault is open. If a fault is (partially) sealing, it will affect the flow and temperature. A sealing fault will break the radial symmetry.

A more severe limitation induced by the radial symmetry and the SRIMA model setup is that a possible vertical offset between reservoir compartments on either side of the fault cannot be incorporated. Fault offset tends to concentrate the shear stress, as is shown in various 2D plane-strain model approaches (Buijze, van den Bogert, Wassing, & Orlic, 2019). In particular, when the pressure or temperature changes outside the reservoir are zero, stress concentrations develop at the reservoir corners. However, when temperature or pressure diffusion to the seal and base is considered, as is done in SRIMA, these stress concentrations become smoother and the effect of offset on the shear failure potential becomes reduced (section A.1.3). For steep dips (>70°), the offset still influences the failure potential. However, most normal faults have orientations less than this, in the order of 60°, so the effect of offset on stress changes may be limited and SRIMA will to a first order capture the thermo-elastic stress changes. It is recommended that in the future a rigorous investigation into the effect of offset is made under a wide range of parameters, and a correction on the stress changes is applied where needed.

The second symmetry choice is that pressure increase and temperature change in the injection layer are taken independent of vertical position. For relatively thin and homogeneous layers this approximation is justified: the influence of seal and base on these fields is only limited. For reservoir layers thicker than 300 m and layers with vertical heterogeneity, the approximation is not always warranted. Heating of the injected fluid in the injection layer may not be distributed over its full height and channeling may cause thinner cooled regions reaching further into the reservoir.

The pressure distribution can be complicated due to the well completion. In the case of a limited perforation interval, the pressures at the upper and lower reservoir boundaries are smaller than at the wellbore; at the perforations they will be larger than calculated because of flow contraction. In the case of a deviated wellbore the temperature distribution will be affected for a short time after starting the injection and affect only the pressure distribution closest to the wellbore. For both cases, the effect on the induced stresses at distances of a limited number of wellbore radii away will be very limited.

Furthermore, geothermal projects typically consist of both an injection and a production well. The effect of the producer on the pressure field around the injector will become sizeable on distances from the injection well that are of the order of half the well distance. The cooled volume will develop a drop shape towards the production well. However, perpendicular to the doublet orientation the radial symmetric assumption of only the injection well will be an adequate approximation (Buijze et al., 2021). Therefore, for a doublet oriented parallel to major fault structures, as most doublets are in the Netherlands, the effect of ignoring the production well on the extent of the cooled volume is minor.

Besides the choice for axial symmetry, the present implementation of SRIMA only considers drained conditions: fluid pressure is controlled by pressure diffusion. For very low permeabilities in seal and base, undrained conditions are prevalent. However, the choice of drained conditions in seal and base will usually be conservative if there is cooling, because the undrained cooling would decrease the pore pressure and consequently increase the effective stresses. This needs, however, to be corroborated through more elaborate research, considering the contributions of all stress components and the full coupling between temperature, pressure, and stress.

Finally, variations of injection rates or temperatures cannot be captured with the analytical correlations that we use. To have some grip on the effect of these variations we calculate the temperature distribution and the associated thermoelastic stresses with the average injection rate, while we use the maximum rate for the calculation of pressures and associated poro-elastic stresses.

2.1.2 Temperature distribution

Injection into the reservoir involves thermal effects through convection and conduction. The differential equation describing the temperature T reads (Nield & Bejan, 2006).

$$(\rho C)_{\text{rock}} \frac{\partial T}{\partial t} + (\rho C)_{\text{fluid}} \mathbf{v} \cdot \nabla T = \nabla \cdot (K_{\text{rock}} \nabla T) \qquad 1$$

with ρ the density; C the specific heat; $\mathbf{v}$ the superficial fluid velocity; K the heat conductivity, and t time. The subscript "rock" refers to the fluid-filled matrix; the subscript "fluid" to the injected fluid. This equation assumes equal temperature of the fluid and the solid where they are in contact.

Mossop (2001) formulated a solution to the diffusion-advection equation in a system with purely radial-horizontal convection in a advection-dominated permeable layer or horizontal fracture, and purely vertical diffusion in the low-permeability overlying and underlying layers. The equations were independently developed by Barends (2010). Candela, Van der Veer, & Fokker (2018) also used this formulation.

The solution for the temperature in the seal, T_{seal}, and in the reservoir, T_{aq}, with layer of thickness h (centered around z=0) in which a relatively cool fluid is injected with a mass injection rate $\dot{m}$ from time t=0 onward reads:

$$T_{seal}(r,z,t) = T_0 + \Delta T_0 \operatorname{erfc}\left[\frac{ar^2 + b\left(|z| - \frac{h}{2}\right)}{\sqrt{t - cr^2}}\right] H(t - cr^2)$$

$$T_{aq}(r,t) = T_0 + \Delta T_0 \operatorname{erfc}\left[\frac{ar^2}{\sqrt{t - cr^2}}\right] H(t - cr^2)$$

$$a = \frac{\pi K_{\text{rock}}}{\dot{m} c_{\text{w}} \sqrt{\kappa_{\text{T}}}}; b = \frac{1}{2\sqrt{\kappa_{\text{T}}}}; c = \frac{\pi h \xi \rho_{\text{fluid}}}{\dot{m}}$$

$$\kappa_{\text{T}} = \frac{K_{\text{rock}}}{(\rho C)_{\text{rock}}}; \xi = \frac{(\rho C)_{\text{rock}}}{(\rho C)_{\text{fluid}}} \qquad 2$$

Here, T_0 is the initial temperature, ΔT_0 is the difference between the initial temperature of the rock and the injection fluid. H is the Heaviside function, r is the radial distance from the wellbore, z the vertical position, t is time since the start of injection, κ_{T} is the thermal diffusivity, ρ, K and C are density, thermal conductivity and heat capacity.

For sandstone, κ_{T} typically ranges between 4x10^{-7} m^2/s (Carslaw & Jaeger, 1992) to 1x10^{-6} m^2/s (Grant (2013), p.305). A characteristic sandstone reservoir in the Netherlands has a κ_{T} of 7x10^{-7} m^2/s (from K=2.5 W/(m.K) with ρ=2400 kg/m^3 and C=1500 J/(kg.K)).

The solution in the seal at radial distances close to the wellbore is approximately

$$T_{\text{seal}}(r \approx 0, z, t) - T_0 = \Delta T_0 \operatorname{erfc} \frac{z - \frac{h}{2}}{2\sqrt{\kappa_{\text{T}} t}} \qquad 3$$

2.1.3 Pressure distribution

The pressure associated with injection of water into an aquifer depends on a number of parameters: injection rate, time elapsed, aquifer permeability and -height, skin, water viscosity of cold (injected) and warm (reservoir temperature) water, distribution of reservoir properties, well configuration and porosity (Dake, 1983).

In a permeable aquifer, a pressure distortion will quickly propagate into the reservoir and the pressure profile around an injection well will become approximately logarithmic (Dake, 1983). With a diffusivity of typically 0.1 m^2/s for a 10 mD reservoir, one day of injection will already result in a logarithmic pressure profile extending to a radius of more than 100 m. If we have obtained a steady-state pressure distribution with negligible leakage to overlying and underlying layers, with a constant-pressure boundary at a distance r_e, and constant viscosity μ, the pressure distribution in the reservoir $P_{\mathrm{aq}}(r)$ is given by

$$P_{aq}(r,t) = \begin{cases} P_0 + \dfrac{\dot{m}\mu_h}{2\pi\rho_w k_{aq} h}\ln\dfrac{r_e}{r} & (r > r_c) \\ P_0 + \dfrac{\dot{m}\mu_h}{2\pi\rho_w k_{aq} h}\ln\dfrac{r_e}{r_c} + \dfrac{\dot{m}\mu_c}{2\pi\rho_w k_{aq} h}\ln\dfrac{r_c}{r} & (r \le r_c) \end{cases} \quad 4$$

P_0 is the original reservoir pressure; $\dot{m}$ the mass injection rate; ρ_{w} the density of the injected water; k_{aq} the permeability and h the height of the injection layer. The radius r_c indicates the thermal front and is taken as the distance from the well where the temperature has decreased to 50% of the total decrease. The viscosities for the hot and cold reservoir parts are μ_h and μ_c.

Due to the low permeability in the adjacent layers (seal and underburden), the pressure distribution there is not stationary. For drained conditions it must be determined through the application of Darcy flow and mass balance. This pressure is also described by a diffusivity equation:

$$\begin{gathered} \frac{\partial P}{\partial t} = \kappa_{\mathrm{P,z}}\frac{\partial^2 P}{\partial z^2} + \kappa_{\mathrm{P,r}}\frac{\partial^2 P}{\partial r^2}\left(t \ge 0; |z| \ge \frac{h}{2}\right) \\ P\left(z > \frac{h}{2}, t = 0\right) = P_0 \\ P\left(z = \frac{h}{2}, t\right) = P_{\mathrm{aq}}(r) \end{gathered} \quad 5$$

The hydraulic diffusivity $\kappa_{\mathrm{P}} = \frac{k_{\mathrm{seal}}}{\phi\mu c}$ in which k_{seal} is the permeability; ϕ the porosity; μ the viscosity and c the compressibility. The value may be different for horizontal and vertical directions due to permeability anisotropy. A very small permeability of 0.00003 mD = 30 nd = 3x10^{-20} m^2 (viscosity of 1 cP; porosity of 10%) already results in a diffusivity of 6x10^{-7} m^2/s, comparable to the value of the thermal diffusivity. This solution is not valid in the case of relatively large permeability in the bounding layers above and below. More research should be performed to formulate a threshold for that value, but we think a ratio between the reservoir and the bounding layers of 10^{-4} should be sufficiently small as threshold for the validity of the approximation in most cases. In addition, more research is required to formulate a condition for undrained conditions, especially when temperature changes induce pore pressure changes that cannot be alleviated by pressure diffusion. Also, a measure is necessary that quantifies whether drained or undrained conditions are more appropriate model choices.

In contrast to thermal diffusion, a simple 1D diffusion into seal and base will not work for the pressure. The reason is the large variation of the pressure close to the well. Pressure that is induced in the seal near the well bore will “leak away” both vertically and horizontally, and the second term in the pressure diffusion equation cannot be discarded. Alternatively, one can state that the pressure in the seal at some distance is influenced by an extended pressurized area of the reservoir. We therefore adopted an equation similar to the expression for temperature but with the temperature substituted by an effective pressure for such a cylinder in the reservoir. The size and the pressure of the cylinder have been benchmarked with the numerical validation calculations (Section 2.2.4).

$$P(r,z,t) = P_0 + \left(P_{aq}(r,t) - P_0\right) \operatorname{erfc} \frac{z - \frac{h}{2}}{2\sqrt{\kappa_P t}} \quad 6$$

For the diffusivity in the seal and the base we take the value as calculated for the virgin reservoir temperature. This will result in an overestimate of the pressure close to the well and close to the interface. In addition, as stated earlier, undrained effects in the seal, due to cooling, are not considered. This also leads to an overestimation of pressures in the seal.

2.2 Mechanical model

2.2.1 Basic assumptions

Induced stresses are calculated with approximations for linearly elastic material, including poro-elasticity and thermo-elasticity (Fjaer et al., 2008). The evaluation of stresses based on the temperature and pressure build upon the work of Myklestad (1942) and Perkins and Gonzalez (1985).

The induced stresses are added to the virgin in-situ stresses, which may exhibit stress gradients, contrasts in horizontal stresses at the reservoir upper and lower boundaries, and horizontal stress anisotropy. The induced stresses are radially symmetric as are the pressure and temperature fields that cause them, but anisotropy of the initial stress will result in radially anisotropic total stresses.

SRIMA does not consider wellbore stability. The mere presence of the well changes the stress distribution around it (Kirsch, 1898). However, the main influence of these concentrations is limited to a few borehole radii away from the well. Since we focus on hydraulic fracturing and fault reactivation in the reservoir and seal somewhat away from the well, we discard the stress concentrations at the wellbore. We thus consider the effects far enough from the well to discard stress concentrations at the wellbore, but close enough to discard the radial decrease of induced stresses.

Linear poro-thermo-elasticity can strictly only be employed when failure does not occur. Up to failure conditions, however, the calculations are trustworthy. This is the case for most of the rock mass under study, also when there are differences in elastic modulus between the reservoir and the bounding layers. We have demonstrated that the approximations are acceptable as long as the value of the elastic modulus of the bounding layers is within a quarter and 4 times the modulus in the reservoir. (Section A.1.2). Larger contrasts are rare when assuming a realistic range of Young's moduli for various rock types.

The coupling between pressure, temperature and stresses is a one-way coupling. As an example, pressures induced by strains that originate from stresses induced by temperature changes are not considered. However, the two-way coupling effect are usually only relevant on small scales, close to interfaces between layers or on places where variations in temperature and pressure are large. Only the possible confined behaviour in a very low-permeability seal and underburden may warrant further investigations – however the present treatment is conservative for cooling.

2.2.2 Poro-thermo-elastic equations

When the temperature and pressure distributions (in terms of their change from initial values, ΔT and ΔP) are known and the mechanical behavior is linearly elastic, the induced stresses and strains ($\Delta\sigma_{ij}$ and ε_{ij},) and the volumetric strain ε_{v} must obey the poro-thermo-elastic constitutive equation. Selecting the sign convention with compressive stresses positive, we have:

$$\Delta\sigma_{\mathrm{ij}} = 2G\left[\varepsilon_{\mathrm{ij}} + \frac{\nu}{1-2\nu}\varepsilon_{\mathrm{v}}\delta_{\mathrm{ij}}\right] + (\alpha_{\mathrm{Biot}}\Delta P + \beta_{\mathrm{T}}\Delta T)\delta_{\mathrm{ij}} \quad 7$$

Here, G is the shear modulus; ν the Poisson ratio, α_{Biot} is Biot constant, $\beta_{\mathrm{T}} = \alpha_{\mathrm{b}} K = 3\alpha_{\mathrm{T}} K = \frac{\alpha_{\mathrm{T}} E}{1-2\nu}$ the product of the volumetric thermal expansion coefficient α_{b} times the bulk modulus K; α_T the linear thermal expansion coefficient. We further define for later use the thermo-elastic (A_T) and poro-elastic stress (A_P) path parameters

$$A_{\mathrm{T}} = \frac{1-2\nu}{1-\nu} \cdot \beta_T = \frac{E\alpha_{\mathrm{T}}}{1-\nu}$$
$$A_P = \frac{1-2\nu}{1-\nu} \alpha_{\mathrm{Biot}} \qquad 8$$

Eq. 7 needs to be solved with the appropriate boundary conditions; pressure and temperature changes will induce poro-elastic and thermo-elastic strains and stresses.

2.2.3 Thermo-elastic stresses

For a cooled cylinder with a discontinuous temperature profile at the boundary, analytical equations are available for the induced thermo-elastic stresses, both inside and outside the cooled cylinder (Myklestad, 1942; Perkins & Gonzalez, 1985). These can be easily implemented (Candela et al., 2018). We have discretized the temperature profile in the reservoir in 10 steps of equal temperature change and calculate the contribution of each of the resulting cylinders to the stress.

Besides the cooled part of the reservoir, there is also cooling of part of the seal and the base. For the effect of this zone, we assume a uniaxial stress change $A_{\mathrm{T}}\Delta T$ at each point in the seal and base. Outside, it is approximately zero. Vertical induced stresses are zero both inside and outside such cylinders. These equations follow from the Myklestad solutions for a very flat cooled cylinder, i.e., a cylinder with a large radius / height ratio, and at radial locations well within the cooling radius. The uniaxial solution was chosen because in most cases the assumption of flatness is valid, and no discretization of the region (which would introduce another approximation and discontinuities) then is required.

Myklestad developed his equations for a cooled or heated cylinder in a full space with homogeneous elastic properties. Realistic geological scenarios require the possibility of incorporating inhomogeneities. For the thermo-elastic stresses these would be properties that are different for different layers. We applied the analytical correlations developed for homogeneous subsurface to situations with an elasticity contrast between reservoir and seal and base, but with dedicated A_{T}: for thermoelastic stresses in the reservoir we take the reservoir value; for thermo-elastic stresses in the seal and base we take the seal and base values when calculating the horizontal components and the value for the reservoir for the vertical components. This was based on a benchmark exercise. Results of the validation are given in Section A.1.2.

Our estimate for the thermal stress is therefore Myklestad's solution both inside and outside the cooled cylinder in the reservoir, supplemented with a term proportional to the temperature change at positions outside that region.

2.2.4 Poro-elastic stresses

Poro-elasticity and thermo-elasticity have similar effects on the total stress changes (Geertsma, 1957; Wang & Dusseault, 2003) but have a different effect in terms of effective stress because of the direct effect of pressure to the effective stress). However, the input distribution of temperature and pressure in our system is very different, therefore a different treatment is required. Notably, the pore pressure in the reservoir is a logarithm function of the distance from the well. An obvious approach would therefore be to discretize the pressurized area and numerically integrate the contribution of pressurized "ring elements" to the poro-elastic stress (Geertsma, 1973). Such approach is beyond the scope of our current setup. We have chosen to approximate the effect of the complete pressurized reservoir with the effect of a single pressurized cylinder. The pressure and the radius of this cylinder depend on the

position where we want to evaluate the stresses. Clearly, a calibration is crucial in this approach.
The best approximation that we found, in terms of simplicity and accuracy, uses an equivalent pressurized cylinder, r_{eq}, defined as radius $r_{\mathrm{eq}} = 10r$ and an equivalent pressure, ΔP_{eq}, given by $\Delta P_{\mathrm{eq}} = \Delta P\left(\frac{1}{10}r_{\mathrm{eq}}, 0\right)$ for the poro-elastic effect at a position (r, z); $|z| \leq \frac{h}{2}$ in the reservoir. In the seal and underburden r_{eq} becomes $r_{\mathrm{eq}} = 10r + \left(|z| - \frac{h}{2}\right)$ and the equivalent pressure is given by $\Delta P_{\mathrm{eq}} = \Delta P\left(\frac{1}{10}r_{\mathrm{eq}}, 0\right)$ for the poro-elastic effect at a position (r, z); $|z| > \frac{h}{2}$. Figure 2visualizes the concept for the equivalent pressurized cylinder. The factor $A_{\mathrm{T}}\Delta T$ that is present in the thermo-elastic expressions is replaced by $A_{\mathrm{P}}\Delta P_{\mathrm{eq}}$.
The effect of the pressurization of parts of the seal and the underburden is treated completely analogous to the thermo-elastic effect of the cooling of those parts: we add a term $\gamma_h \Delta \mathrm{P}$ to the cylinder contribution in the seal and the underburden, with the actual pressure at the point of calculation. The vertical stresses are unchanged.
Introducing elasticity contrasts at the interfaces had only minor effect on the resulting poro-elastic stresses. This is due to the form of stress path coefficients. The elastic modulus is directly present in the coefficient for thermo-elasticity; it is absent in the coefficient for poro-elasticity. Only some effect of the Poisson ratio remains.

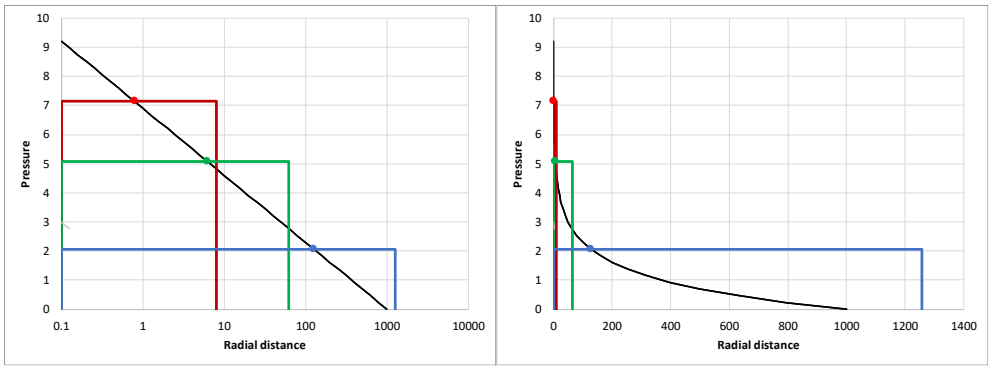

Figure 2 Concept of equivalent pressurized cylinder. The poro-elastic fields at the position of the red, green, and blue dots originates from the pressure in the reservoir that is given by the black curve. It is approximated by Myklestad's correlations for a pressurized cylinder with constant pressure inside it and a radius of 10 times the point of interest: the red, green and blue curves. Left and right show the same curve but with linear and logarithmic distribution of the radial distance

2.2.5 Total stresses

The calculated thermo-elastic and poro-elastic contributions to the stress are radially symmetric. If the virgin horizontal stresses are anisotropic, the rotational symmetry of the end product is broken, and the thermo-elastic and poro-elastic contributions must first be transformed to the cartesian coordinate system (σ_{cart}^{TPE}):

$$\sigma_{cart}^{TPE} = \begin{pmatrix} \sigma_{xx}^{TPE} & \sigma_{xy}^{TPE} & \sigma_{xz}^{TPE} \\ \sigma_{xy}^{TPE} & \sigma_{yy}^{TPE} & \sigma_{yz}^{TPE} \\ \sigma_{xz}^{TPE} & \sigma_{yz}^{TPE} & \sigma_{zz}^{TPE} \end{pmatrix}$$
$$= \begin{pmatrix} \cos\varphi & \sin\varphi & 0 \\ -\sin\varphi & \cos\varphi & 0 \\ 0 & 0 & 1 \end{pmatrix} \begin{pmatrix} \sigma_r^{TPE} & 0 & \sigma_{rz}^{TPE} \\ 0 & \sigma_\theta^{TPE} & 0 \\ \sigma_{rz}^{TPE} & 0 & \sigma_z^{TPE} \end{pmatrix} \begin{pmatrix} \cos\varphi & -\sin\varphi & 0 \\ \sin\varphi & \cos\varphi & 0 \\ 0 & 0 & 1 \end{pmatrix} \quad (9)$$
$$\varphi = \operatorname{atan}\left(\frac{y}{x}\right)$$

This expression makes use of the fact that induced shear stresses along the tangential coordinate must be zero because of the symmetry. The thermo-poro-elastic contributions to the stress are added to the virgin stresses. The virgin stress in cartesian coordinates is obtained through a rotation of the stress in principal value orientation, $\begin{pmatrix} \sigma_{h0} & 0 & 0 \\ 0 & \sigma_{H0} & 0 \\ 0 & 0 & \sigma_{v0} \end{pmatrix}$, over the angle of the direction of the maximum horizontal stress with regard to the north ($\sigma_{h0}, \sigma_{H0}, \sigma_{v0}$ are minimum in-situ horizontal stress, maximum in-situ horizontal stress and in-situ vertical stress)

2.3 Fracture extent estimation

We have implemented an estimate of how far a hydraulic fracture could grow. The stresses are determined by the temperature field and the pore pressure. Once a fracture starts developing, however, the pressure in the fracture is not the pore pressure at that location anymore, but it is controlled by the pressure at the injection point. We thus estimate the pressure that would be present in a fracture if it would exist and if there would not be pressure losses due to frictional flow. This pressure, P_{hf}, at depth z, is the calculated pore pressure of fluid entering the injection layer at the wellbore, corrected only for the hydrostatic head originating from the fluid density and the depth difference between injection point and point of calculation:

$$P_{hf} = P_{wb} + (z_{wb} - z)\rho_w g \qquad 10$$

Here, P_{wb} is the fluid pressure when entering the reservoir at the wellbore at depth z_{wb}, ρ_w is the fluid density and g the gravitational acceleration constant. Ignoring the frictional pressure drops in the fracture makes the estimate conservative.

The potential vertical extent of a hydraulic fracture is then calculated as the maximum extent at which this pressure is larger than the minimum in-situ stress plus the fracture overpressure, that is the minimum and maximum depths at which $P_f > \sigma_3 + \Delta P_f$, in which σ_3 is the minimum in-situ stress and ΔP_f the fracture overpressure. The possibility that the in-situ stress σ_3 changes due to the distorted flow pattern is not taken into account – in many cases this effect will be limited since there is not much flow in the fracture interior. The fracture overpressure is the excess pressure required on top of the minimum in-situ stress that is required to propagate a fracture. As such it incorporates the critical stress intensity factor (i.e., the "fracture toughness" in an ad hoc way. Choosing a zero fracture for the fracture overpressure provides a conservative estimate [Roodhart et al, 1995]. Figure 3 demonstrates the concept. How results for tensile failure are handled in stochastic simulations is addressed in Section 2.5.

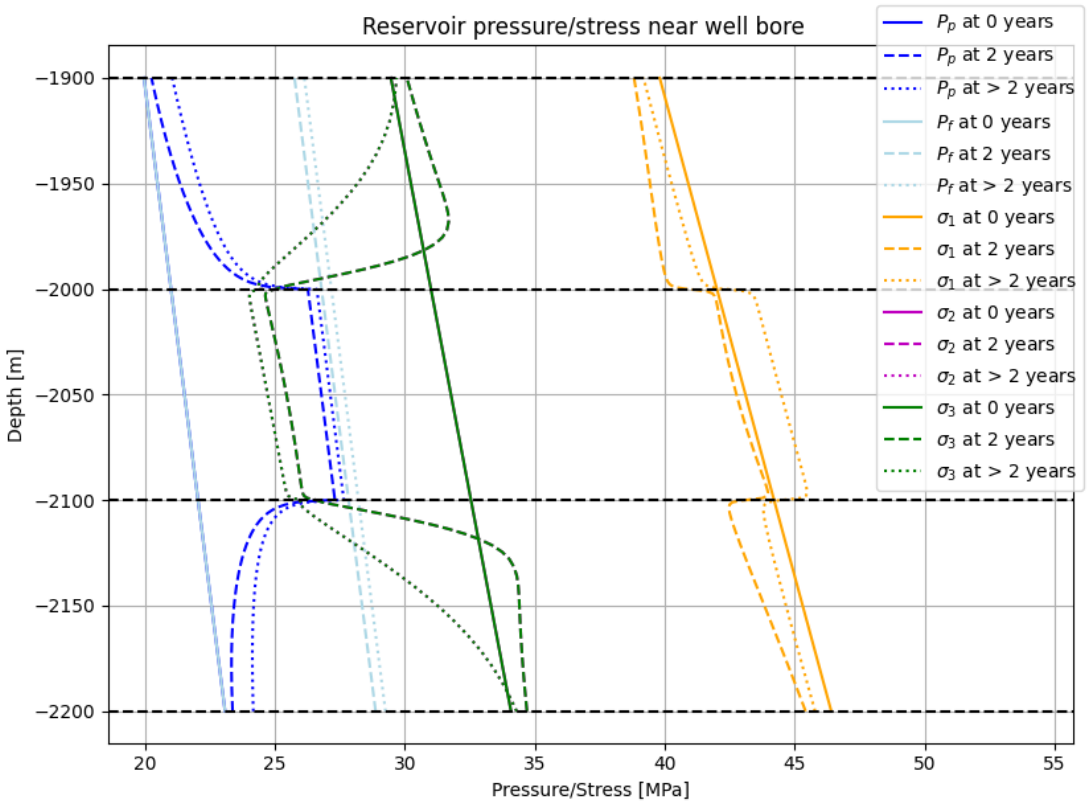

Figure 3 Demonstration of Hydraulic Fracture Potential (with $\Delta P_f = 0$). Significant cooling has decreased the horizontal stresses; pressurization has increased the vertical stress in the reservoir. While the modelled pore pressure decreases rapidly outside the injection layer, the pressure in a potential fracture will be high because of direct hydraulic connection with the wellbore pressure. Hydraulic fractures can develop where the "fracture pressure", P_f, is larger than the minimum in-situ stress σ_3.

2.4 Shear failure estimation

A virtual fault is included in the model geometry with a given dip angle θ and dip direction ϕ (Figure 4). The dip direction is defined with regard to the northern direction. The stresses are defined with respect to the same coordinate system; the initial stresses are dependent on the direction of the maximum horizontal stress σ_H (in case $\sigma_h \neq \sigma_H$). The shear stress and the normal stress on the fault are computed from the traction of the full stress tensor on the fault plane.

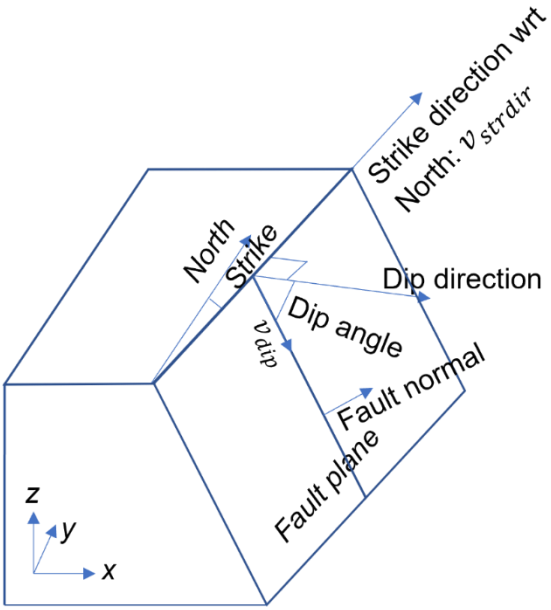

Figure 4 Definition of fault plane. The dip direction is perpendicular to the strike.

The fault normal is defined as

$$\mathbf{n}_{fault} = \begin{pmatrix} \sin\varphi \ \sin\theta \\ \cos\varphi \sin\theta \\ \cos\theta \end{pmatrix} \quad 11$$

Then the traction on the fault (T), and the normal (σ_n) and shear components (τ) of it are given by

$$\begin{aligned} \mathbf{T} &= \sigma \cdot \mathbf{n}_{fault} \\ \sigma_n &= \mathbf{T} \cdot \mathbf{n}_{fault} \\ \tau &= \sqrt{\mathbf{T} \cdot \mathbf{T} - \ \sigma_n \cdot \sigma_n} \end{aligned} \quad 12$$

The Mohr Coulomb failure criterion is assumed for the fault strength

$$\tau_f = \mu(\sigma_n - P_p) + C \quad 13$$

where τ_f is the shear stress at which shear failure occurs, μ is the static friction coefficient, P_P is the pressure at the fault and C the cohesion. The proximity to failure can be expressed as the Shear Capacity Utilization (SCU)

$$SCU = \frac{\tau}{\tau_f} = \frac{\tau}{\mu(\sigma_n - P_p) + C} \quad 14$$

An SCU of 0 indicates the lack of any fault shear stress (stable), and an SCU of 1 indicates the Mohr-Coulomb criterion has been reached and fault slip can occur. Note that fault slip and stress redistribution is not modeled in SRIMA. Therefore, the state of stress can be such that the SCU on the virtual fault is larger than 1.

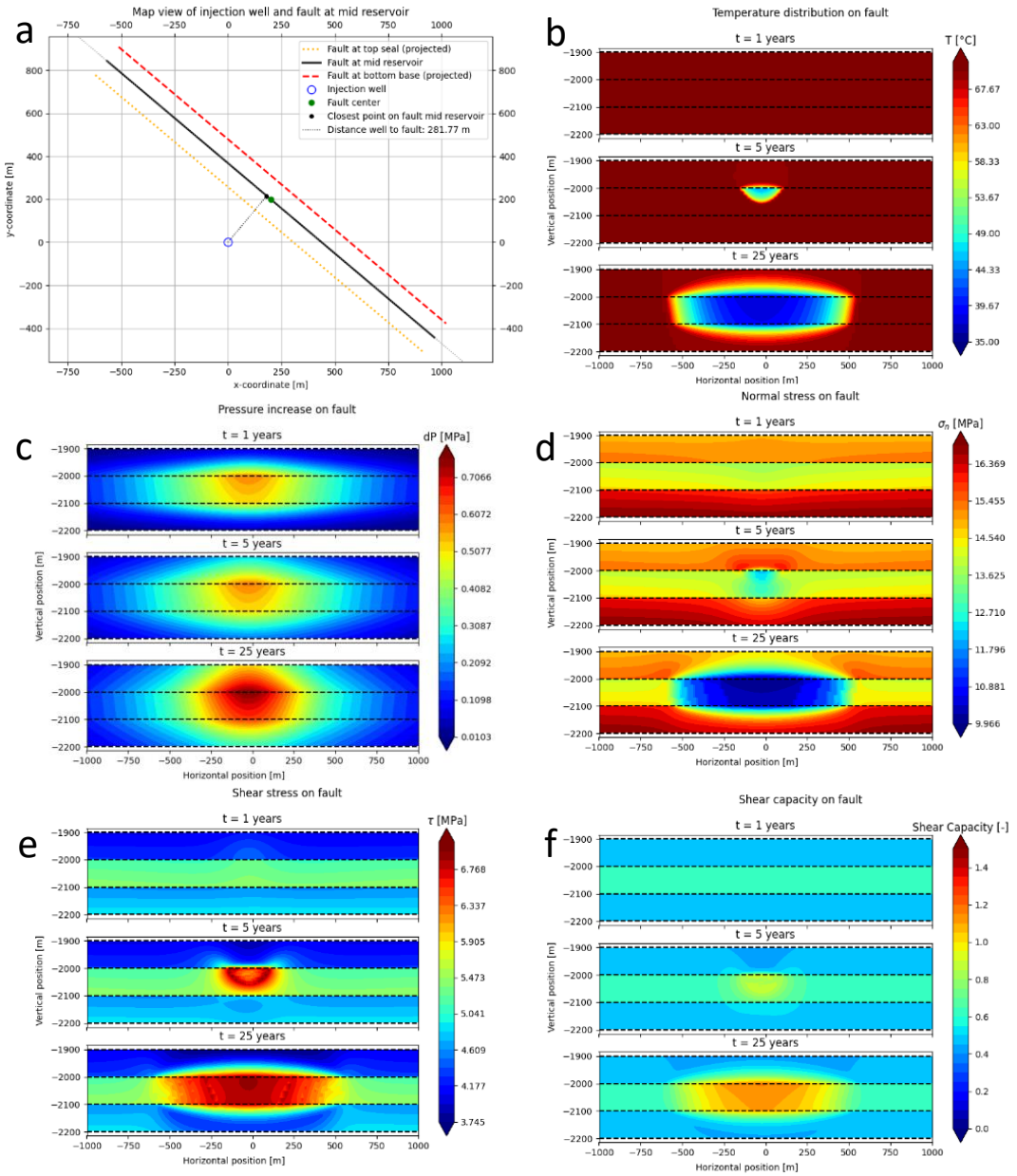

Figure 5 Example temperature, pressure, and stress changes on a fault nearby the injection well, as computed in SRIMA. Results are shown for three timesteps; 1 year, 5 years, and 25 years. Reservoir depth is indicated by the dashed lines (b-f). a) position of injection well and fault, top view, b) temperature changes on fault, c) pressure changes on fault, d) normal stress changes on fault, e) shear stress changes on fault, f) shear capacity utilization (SCU) on fault.

An example of fault stresses computed in a typical model realization in SRIMA is shown in Figure 5. As the cold front (front of the cooled volume) reaches the fault, the normal stress decreases and the shear stress increases. The net effect is an increase in SCU. Note that even before the cold front reaches the fault, small stress changes occur due to elastic stress transfer. The stress signature is dominated by the temperature changes; the pressure is affected mostly near the injection well are pressure changes decay logarithmically with the distance from the injection well (equation 4). The cooled and stressed fault area is wider near the top of the reservoir. This is due to the fault dipping away from the injection well.

When a fault orientation is not known, the slip tendency can be calculated for the fault orientation that is most prone to failure. The calculation does not require stresses for all possible orientations; it suffices to determine the maximum and minimum effective principal stresses σ_1' and σ_3', and the associated shear capacity of the rock, which is a measure for the proximity of the Mohr circle to the failure envelope. The shear capacity utilization for the critical orientation is calculated as

$$SCU = \frac{\sqrt{1+\mu^2}(\sigma_1' - \sigma_3')}{\mu(\sigma_1' + \sigma_3') + 2C} \quad 15$$

Failure will occur if the value for the shear capacity is larger than unity. The measure is defined locally. How results for shear failure are handled in stochastic simulations is addressed in Section 2.5.

2.5 Stochastic model

An important aim of SRIMA is to assess probabilities of failure. Therefore, the implementation has been embedded in a stochastic framework. First, the parameters that are uncertain are identified. Then, many realizations of model parameter sets are created. The parameters are drawn from a bi-triangular probability distribution with an expected value and maximum and minimum values. This way, the expected value has the largest probability.

All realizations are employed in a semi-analytic calculation. The results in terms of pressures, fault activation, hydraulic fractures, are calculated for every realization. The ensemble of realizations thus produces ensembles of values for pressures and failure measures, which can then be used to make probabilistic estimates. Correlations between estimated measures for failure and uncertain input parameters can also be used to steer information gathering. Priority can then be given to information gathering of parameters that have the largest impact on the calculated failure probability.

One assessment of the stochastic results is in the form of so-called cumulative density plots. Consider, as an example, a stochastic run with an ensemble of 2500 calculations performed along a vertical line at the position of the wellbore. We performed calculations after 1, 5, and 25 years of injection. For every output variable we then also have an ensemble of 2500 outcomes for these three times. Figure 6 shows the cumulative occurrence of hydraulic fracture potential and for shear failure extent larger than the value on the horizontal axis. We see that for the three times chosen, the probability for any potential hydraulic fracture in the seal increases from 0.32 to 0.42. The probability of shear fractures is larger, which is understood through the mechanism of shear failure occurring for stresses that are still compressive. Some realizations result in shear failure of the complete 100-m thick seal, even some already early in time, due to critical stressing of the virgin reservoir and seal. The probability of developing larger fractures increases with time. P90, P50 and P10 values can be determined by simple intersection of these curves with the 0.9, 0.5 and 0.1 cumulative probability, Figure 6. The points indicate the probability of 0.9, 0.5, and 0.1 of finding a length larger than the indicated length.

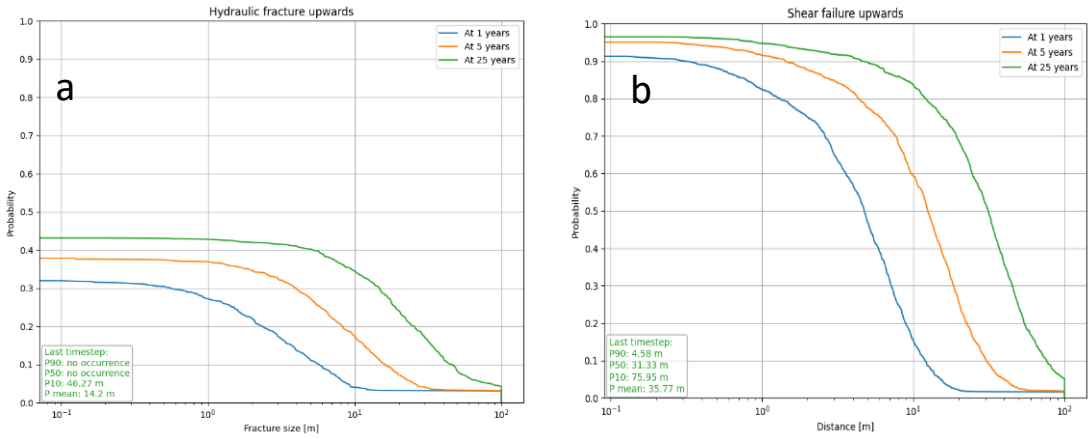

Figure 6 Cumulative density plots for the probability of potential hydraulic fractures larger than a certain size (left) and for the extent of shear failure (right)

Operators also need guidance with respect to allowed injection pressures. A possible question could be "What is the maximum value of the pressure for which the probability of not creating a hydraulic fracture larger than, e.g., 50% of the seal thickness (i.e., the probability that injection is safe) is at least, e.g., 95%." To answer such questions, the stochastic output values for hydraulic fracture height and pressure need to be correlated. The pressure values are grouped in intervals ("bins") with a certain number of realizations, and for each bin the number of fractures staying with the predetermined limit is determined. The average pressure within each bin and the proportion of safe realization are then plotted and fitted to a Gaussian cumulative density function. This allows to determine an estimate of the safe value of the pressure.

The combination of results for tensile failure and shear failure in the stochastic model are best demonstrated through an example. Consider the same ensemble as above. Each of those calculations has an outcome in pressure profile, total stresses, and based on that also creation and extent of hydraulic fracture and shear fracture in seal and base. We can visualize the parameters relevant for the question at hand by plotting the potential vertical extent of a hydraulic fracture against the wellbore pressure of the same realization. The result is a scatter plot, of which an example is given in Figure 7 (top). Every realization corresponds with a point in the Pressure – Fracture potential plot. Clearly, realizations with large fractures into the seal tend to have a larger wellbore pressure. However, this is only a statistical correlation since other input parameters also have their influence. Important other parameters are, for instance, the virgin minimum principal stress and the injection temperature.
A further stochastic analysis is needed. Our approach is to divide the range of possible pressure outcomes in intervals and determine for each of these intervals the probability of exceeding the allowed fracture growth potential. We have chosen to have intervals with approximately the same number of realizations, and approximately the same number of realizations per interval as numbers of intervals themselves. For the ensemble size of 2,500 realizations, we thus have 50 pressure intervals with each 50 realizations. For each of these intervals, we determine the share of "safe" realizations, and we visualize them. The procedure is performed for the bottomhole pressure (BHP) as well as for the excess injection pressure (EIP). For this application both BHP and EIP are defined at mid-reservoir depth and at flowing conditions. The EIP is calculated by subtracting the initial mid-reservoir pressure from the BHP.

The outcome for the two calculations is represented as the dots in Figure 7 (middle) and Figure 7 (bottom).

Finally, a value is sought for the maximum safe pressure. In the example we define the safe pressure as the pressure for which the probability of not creating a hydraulic fracture larger than 50% of the seal thickness is at least 95%. This requires a fit of the scatter points in the two plots to a theoretical relationship. In the absence of further theoretical observations and considering the many uncertain parameters present, a Gaussian distribution is the best choice for this relationship. The cumulative density function of such a distribution has only two free parameters: the center of the distribution, μ, and its width, σ. The Gaussian distribution then is

$$g(x) = \frac{1}{\sigma\sqrt{2\pi}} \exp\left(-\frac{(x-\mu)^2}{2\sigma^2}\right) \qquad 16$$

The cumulative distribution function as we describe it (essentially 1-*cdf*) is

$$1 - cdf = \frac{1}{2}\left[1 - \mathrm{erf}\left(\frac{x-\mu}{\sigma\sqrt{2}}\right)\right] \qquad 17$$

The parameters μ and σ are determined by minimizing the mismatch between the scatter points in Figure 7 (middle and bottom) and the value from Eq. 17. The 95% value for a safe pressure, finally, is determined by the value at which Eq. 17 with the fitted parameters equals 0.95.

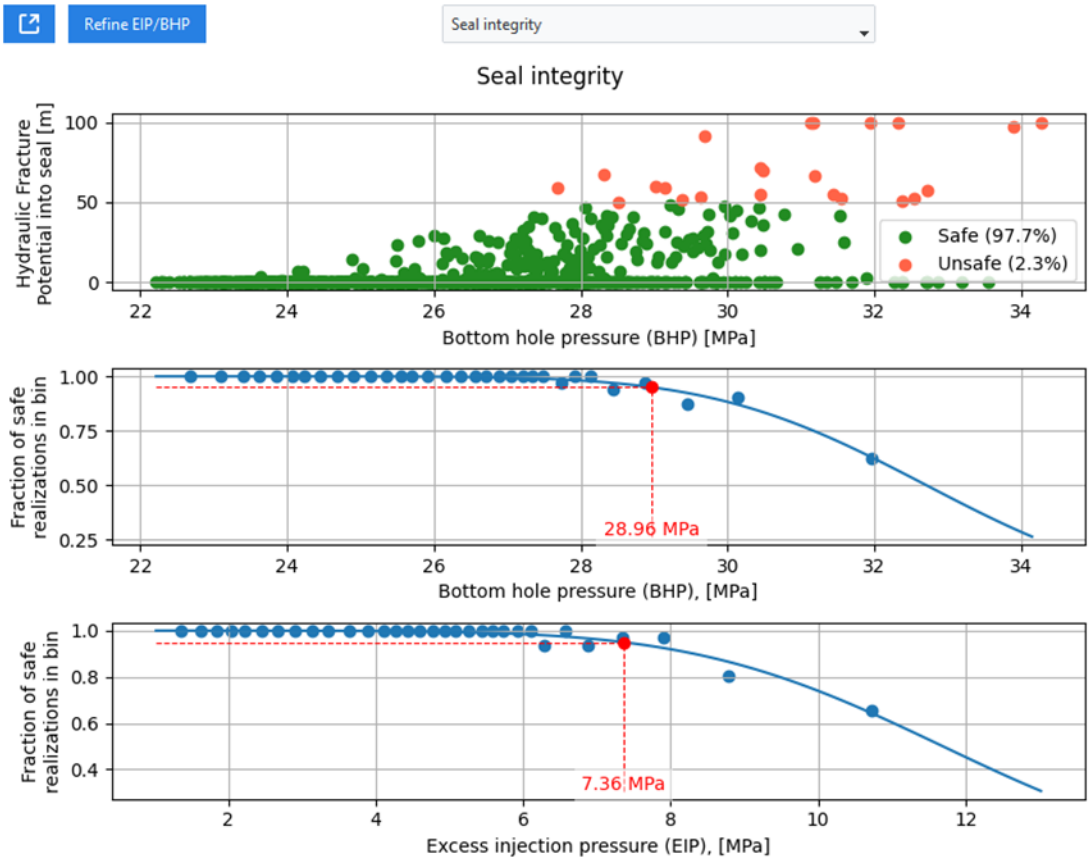

Figure 7 Correlation of hydraulic fracture potential with bottomhole wellbore pressure (BHP) and excess injection pressure (EIP). On the top left there is a Refine EIP/BHP button. This button starts a new calculation based on 10,000 realisations with flow rates that extend the range of flowrates beyond the user defined values. This ensures a more precise and consistent derivation of the p95 safe pressure and results in a new set of graphs. Note however that the plotted points in this new plot should only be used for this purpose.

2.6 Choices for operational parameters

The driving force behind the stress changes and the associated modeled failure is the injection of a fluid of constant temperature at a constant rate. Changing temperatures and rates would preclude the use of analytic expressions, due to the complex interplay between advection in the injection layer and diffusion in the bounding layers. A full realistic injection scheme can therefore not be modelled. For the injection rate, we address this by calculating an increased pressure drop for the maximum rate, as compared to the average rate. The average injection rate will determine the position of the temperature regions and the associated injection fluid viscosity, while the maximum injection rate will determine the pore pressure gradient and the associated pressure drop. Because the calculation of pressure is with semi-steady-state conditions, this is warranted. For the temperature, the approximation gives the first order effect; stochastic calculations can be deployed to map the effect of the temperature range. The thermo-elastic stresses will thus be based on the best estimate of the distribution of the temperature, while the poro-elastic stresses will be based on the maximum injection rate. Care must be exercised, though, since an increased injection rate will increase both the pressure and the poro-elastic contribution to the stress, and the effect on stability depends on the relative changes of both. A user can explore what the effect is of introducing a maximum rate larger than the average injection rate.

2.7 Scenario-based seismic hazard and risk analysis

According to Dutch Mining regulations (MBR) each production license application should contain an analysis of ground motions and Local Personal Risk (see Mijnlieff et al., 2023). This includes a seismic hazard analysis which expresses seismic hazard in terms of ground motions such as peak ground acceleration, PGA, or peak ground velocity, PGV, and gives an indication of damage. For the Seismic Hazard and Risk Assessment for geothermal operations ("*SDRA Geothermie*" in Dutch) the PGV distribution is considered. This ground motion parameter strongly correlates with low levels of building damage (e.g. Damage State 1). One major difficulty with defining a Seismic Hazard and Risk Analysis (SHRA) in the case of geothermal is the lack of seismicity data. Here we adopt a scenario-based hazard analysis, where a largest credible earthquake magnitude (M_{LCE}) is computed on a fault within the cooled region, without knowing its annual probability of occurrence. The chosen approach here has significant implications for the computation of hazard and damage; this will be discussed at the end of this section. The main steps of the SHRA in SRIMA are summarized in

Table 1 and details are explained in the following sections.

2.7.1 Event location

The stressed fault area will be used to compute for the largest credible earthquake magnitude, M_{LCE} (next section). The centre of the stress fault area lies (approximately) at the mid-depth of the reservoir, at the fault location closest to the injection well (Figure 8).

Table 1 Basic steps in the Seismic Hazard Analysis as used in SRIMA

	Steps
Source	A fault intersected by the cold front. The earthquake source is assumed to lie at the point on the fault closest to the injection well.
Seismicity rate	Not considered, but for the damage calculation it is implicitly assumed the Largest Credible Earthquake occurs once over the project lifetime.
Maximum Magnitudes	Largest Credible possible Earthquake (LCE). Here: LCE based on fault area affected by the induced stresses, as computed in SRIMA. This is not a single LCE, but a distribution of LCEs following from the stochastic analysis in SRIMA (section 2.5). The magnitude of this event is termed M_{LCE}.
Ground motion	BMR2 (Ruigrok & Dost, 2020) GMPE model, including the uncertainty, is used to compute the PGV values for each LCE of M_{LCE}.
Hazard	PGV distributions for each M_{LCE} combined to compute probability of exceedance. The Pmean values (at the epicenter) are used to characterize seismic hazard. In addition, the probability of exceedance curve is given for 3 mm/s, also for Pmean. 3 mm/s is used as this is the lower limit value for which damage can occur to brickwork (SBCRURnet, 2017)
Damage	Empirical fragility functions (cf. Crowley et al., 2019) are used to calculate the probability of exceeding Damage State 1, depending on the PGV distribution. Results are aggregated to an average exceedance probability per building within the 3 mm/s contour.

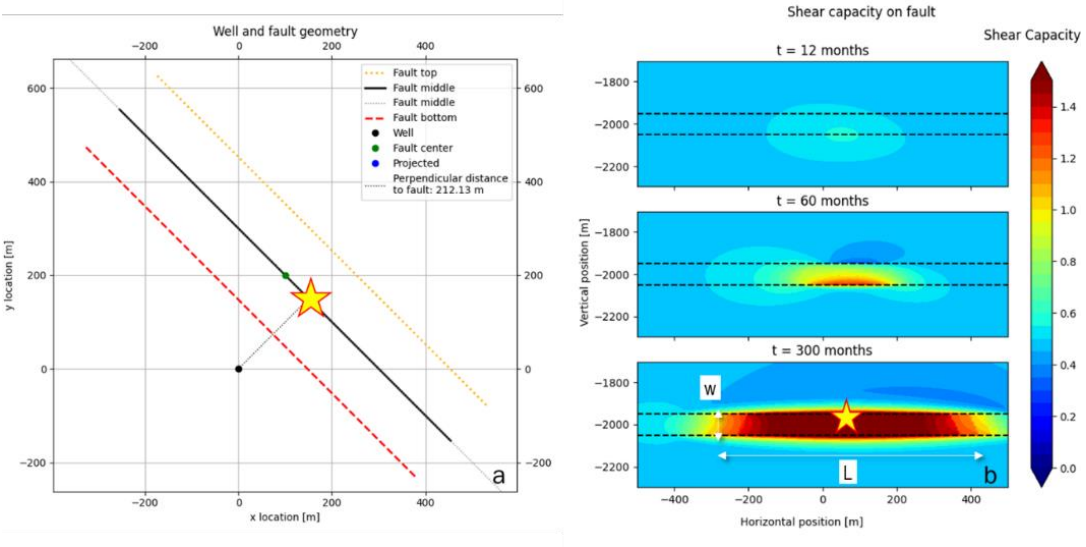

Figure 8 Illustration of where the source location is taken, using default results from SRIMA v1.0.0. a) Top view of the injection well and fault. b) On-fault view of the shear capacity utilization (SCU) indicative of the slip zone (SCU≥1). Hypocenter location is indicated with the star.

2.7.2 Largest Credible possible Earthquake (LCE) magnitude

The results from SRIMA are used to estimate the largest credible earthquake magnitude M_{LCE}, which is used in the SHRA. Modeling of fault slip, dynamic rupture and/or modeling of seismicity rates are beyond the scope of a simplified and easy-to-use tool like SRIMA, and moreover, monitoring data to validate such computations are not available. Hence, seismic slip and magnitudes of seismic events are not explicitly modeled. Instead, the fault area affected by the geothermal operations is used as a proxy for the fault area linked to the largest credible earthquake magnitude. This estimate is comparable to the estimates of M_{max} for the small gas fields (SodM, 2016). Hence, in the end the dimensionality of the area and volume affected by a project imposes a key signature on the M_{LCE} and resulting hazard and damage.

The area A of the part of the fault over which slip occurs (slip zone) is an important ingredient determining the seismic moment, which is indicative for the size of an earthquake (Aki, 1966):

$$M_0 = GAd \qquad 18$$

The seismic moment furthermore depends on the shear modulus of the surrounding rock G and the average fault slip d within the slip zone. Through elastic dislocation theory, the slip within the slip zone can be related to the static stress drop $\Delta\tau$ – i.e., the difference between the shear stress before and after the (seismic) slip event averaged over the slip zone. Using this relation, the seismic moment equation can be rewritten to (Kanamori & Anderson, 1975)

$$M_0 = \left(\frac{\tilde{L}}{C}\right) A\Delta\tau \qquad 19$$

Where C is a proportionality factor close to 1, depending on the fault geometry, and $\tilde{L}$ is the characteristic fault dimension, which also depends on the geometry (e.g., $\tilde{L}$ is the radius for a circular fault slip zone, and width w for dip-slip fault slip zones). For buried dip-slip faults (normal faults) as representative for faulting in the Netherlands, the corresponding seismic moment M_0 [Nm] is given as (Kanamori & Anderson, 1975; Starr, 1928)

$$M_0 = \frac{3\pi}{8}\Delta\tau w^2 L \qquad 20$$

assuming both Lamé parameters are equal (dynamic ν = 0.25). Where L is the along-strike dimension of the slip zone and w is the along-dip dimension of the slip zone, i.e. for a vertical fault the w would be the depth interval of the slipping zone. Note the square dependency on the slip zone width. The seismic moment can be converted to a moment magnitude M_w through (Hanks & Kanamori, 1979)

$$M_w = \frac{2}{3}\left(\log_{10}(M_0) - 9.1\right) \qquad 21$$

The moment magnitude M_w has an approximate 1:1 scaling with the empirical local magnitude M_L or Richter magnitude, which was traditionally used to denote earthquake size. However, (small) differences may exist between the two scales depending on earthquake magnitude, with e.g., a M_w being 0.2 smaller than M_L for Groningen earthquakes with magnitudes 2.5 – 4 (Dost, Edwards, & Bommer, 2016).

We base our estimates of the along-dip and along-strike dimensions of the slip zone on the fault area affected by the geothermal operations, comparable to what is done for the small gas fields. Whereas for the small gas fields the intersection of the largest fault with the gas-filled parts of the reservoir is taken as the affected fault area, here the affected fault area is determined using a stress criterion. To distinguish the magnitude computed here from maximum magnitudes as typically determined from e.g., the truncation of the Gutenberg-Richter frequency-magnitude relationship or the upper bound to recurrence curves, we name the magnitude of the largest credible earthquake M_{LCE}.

M_{LCE} is computed from the calculated fault stresses as follows. For each iteration, for a given timestep, the computed SCU distribution (Equation 14) on the fault plane is considered.

- The slip zone is then defined as the fault area where SCU ≥ 1.
- The slip zone width w is defined as the average of the along-dip fault length within the slip zone where SCU ≥ 1.
- The slip zone length L is defined as the average of the along-strike length within the slip zone where SCU ≥ 1.

Furthermore, the stress drop is needed to compute the magnitude (Equation 20). Since fault slip and frictional weakening are not modeled in SRIMA, the stress drop must be prescribed or computed in a different manner. There are two options:

- A constant stress drop over the slip zone can be prescribed by the user
- Stress drop can be computed by SRIMA at each cell within the slip zone and averaged over the slip zone. Stress drop is computed by taking the difference between the shear stress at which the failure criterion is exceeded, and the residual shear stress computed using a residual friction of 0.3. This value is based on experimental work by Hunfeld et al. (2021).

The resulting magnitude can be computed using Equations 20 and 21.

For the example shown in Figure 9, the average along-dip fault length w is 104 m, and the average along-strike fault length is 244 m. For a stress drop of 5 MPa (the value used for the small gas fields) the resulting seismic moment is $1.6 \cdot 10^{13}$ Nm and the corresponding M_w is 2.7.

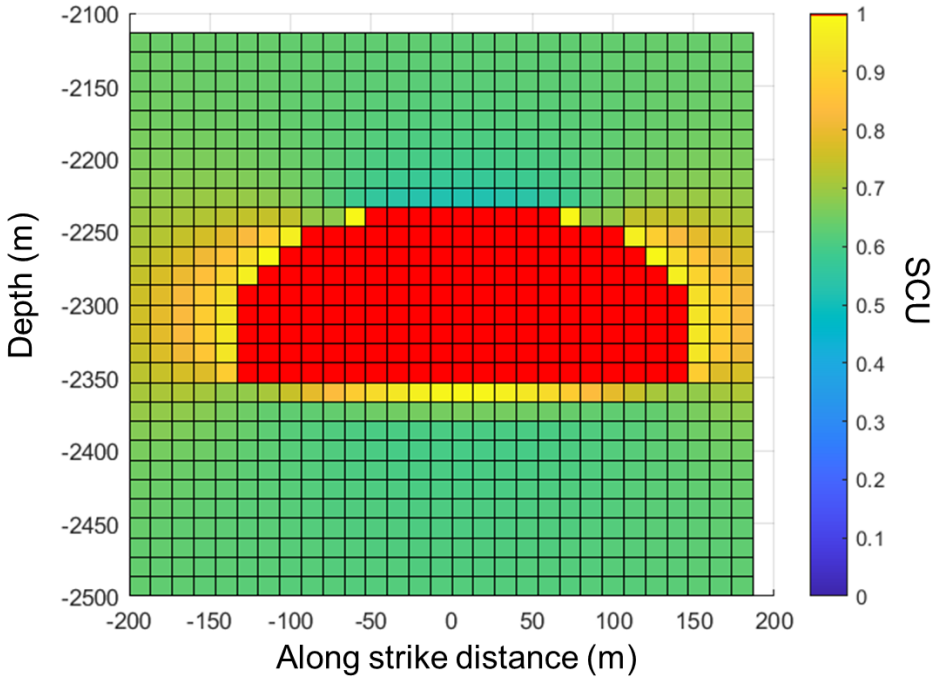

Figure 9 Example of determining the area from SRIMA. In the plot computed SCU values on the fault plane are shown, with red SCU ≥ 1.

Various assumptions underlie this approach:

- (conservative) it is assumed that all the fault slip within the slip zone is *seismic* slip. However, part of the deformation on the fault may be accommodated as aseismic slip. When more data becomes available in the future, it is recommended to better constrain the aseismic/seismic partitioning of induced fault slip.
- (Not conservative) fault slip and resulting stress transfer is not modeled in SRIMA. Taking into account fault slip and stress redistribution would lead to a larger fault area where SCU equals 1. However, the effect on magnitude is likely small because of the logarithmic dependence of magnitude on moment and area. In future models, the effect of fault slip on the perturbed zone could be accounted for, or an SCU threshold of e.g., 0.9 could be assumed to account for this effect.
- (Not conservative) it is assumed slip cannot propagate far beyond the stressed fault area. Such an assumption is deemed valid for a low-stress environment, which is typically assumed for the upper sedimentary formations (and in particular clay-rich or evaporite-rich caprocks and base rocks) of the Dutch subsurface (Bakx, Buijze, & Wassing, 2022).
- (conservative) another assumption is that the stress build-up on the fault is released in a single event. This is regarded conservative; given the gradual buildup of stress on the fault, progressive fault reactivation through multiple smaller events is more likely.
- furthermore, it is assumed that the slip zone can be confined to a finite size fault. If a fault terminates within the cooled and stressed rock volume around the injection well, the fault terminus is considered the endpoint for the along-strike slip zone length.

The stress drop has a big impact on the computed magnitude (Equation 20). The current calculation of stress drop in SRIMA results in lower stress drops (mostly 1 - 5 MPa) compared to the stress drop of 5 MPa used for the small fields. This can be justified as depletion and the

reduction of pore pressure leads to a more compressive state of stress, for geothermal sites cooling may lead to a less compressive state (see e.g., Buijze et al., 2023), so less stress is available. When more (micro)seismic observations become available in the future, it is recommended to build a stress drop database with which the SDRA can be informed further.

2.7.3 Peak ground velocity: BMR2 GMPE

After computing the largest credible earthquake magnitude for different timesteps in each model iteration, the distribution of corresponding peak ground velocities (PGV) is computed. To translate magnitude to ground motion, ground motion prediction equations (GMPE) are required. Here we use the BMR2 GMPE model that has been developed for small earthquakes outside of the Groningen field (Ruigrok & Dost, 2020). This model has been derived on the basis of recorded PGV values resulting from M 1.5 – 3.5 induced earthquakes in the Netherlands occurring outside of the Groningen field. The PGV values are taken from the horizontal recordings of a seismic station. There are three definitions for the PGV:

- PGV_{geo}: the geometric mean of the absolute values of the two horizontal components.
- PGV_{max} : the maximum absolute value of either one of the two horizontal components.
- PGV_{rot}: the combination of the two components to compute the maximum value in the horizontal plane.

The order of the definitions is $PGV_{geo} < PGV_{max} < PGV_{rot}$, and in the SDRA we will use the PGV_{rot} value as it is indicative for the magnitude for the actual PGV and it is the most conservative value. From now on we use PGV as relating to PGV_{rot}.

The BMR2 model is a modification of the Bommer model, which was developed specifically for the Groningen field (Bommer et al., 2019). The Bommer model yielded the best fit with the PGV database for values outside Groningen, compared to three other GMPE models (Ruigrok & Dost, 2020). Only in the first few kms from the source the Bommer model tended to overestimate the ground motions. To reduce the misfit, the Bommer model was adapted to include the hypocentral depth in the computation of the source-site distance term; the adapted model is called the BMR2 model.

The Bommer and BMR2 (Ruigrok & Dost, 2020) models are parameterized as

$$\ln(PGV) = c_1 + c_2 M + g(R^*) \quad (22)$$

Where M is the magnitude, $g(R^*)$ is a geometrical spreading term, which is a function of the point-source distance R^*, which for the BMR2 model is

$$R^* = \sqrt{R^2 + D^2 (e^{\epsilon_1 M - \epsilon_1})^2} \quad (23)$$

with epicentral distance R and event depth D. The geometrical spreading term is split over 3 distance ranges:

$$g(R^*) = c_4 \ln(R^*) \qquad R^* \leq d_1 \quad (24)$$

$$g(R^*) = c_4 \ln(d_1) + c_{4a} \ln\left(\frac{R^*}{d_1}\right) \qquad d_1 < R^* \leq d_2 \quad (25)$$

$$g(R^*) = c_4 \ln(d_1) + c_{4a} \ln\left(\frac{d_2}{d_1}\right) + c_{4b} \ln\left(\frac{R^*}{d_2}\right) \qquad R^* > d_2 \quad (26)$$

The coefficients for the PGV_{rot} are summarized in Table 2. The uncertainty in these PGV values is given by an intra-event standard deviation ϕ of 0.53613, an inter-event standard deviation τ of 0.25242, and a total standard deviation σ of 0.59268 (all given in ln(PGV)).

An example of the PGV and uncertainty bounds with epicentral distance is shown in Figure 10a. The effect of the three different geometrical spreading functions is clearly visible as 'kinks' at 8.1 and 11.6 km.

Table 2 Coefficients for PGV_{rot} for the BMR2 GMPE model.

Coefficient	Value	Unit	Coefficient	Value	Unit
c_1	2.2800	-	ϵ_1	0.0600	-
c_2	2.2835	-	ϵ_2	1.1300	-
c_4	-4.2800	-	d_1	8.10	km
c_{4a}	-0.8000	-	d_2	11.62	km
c_{4b}	-1.7000	-			

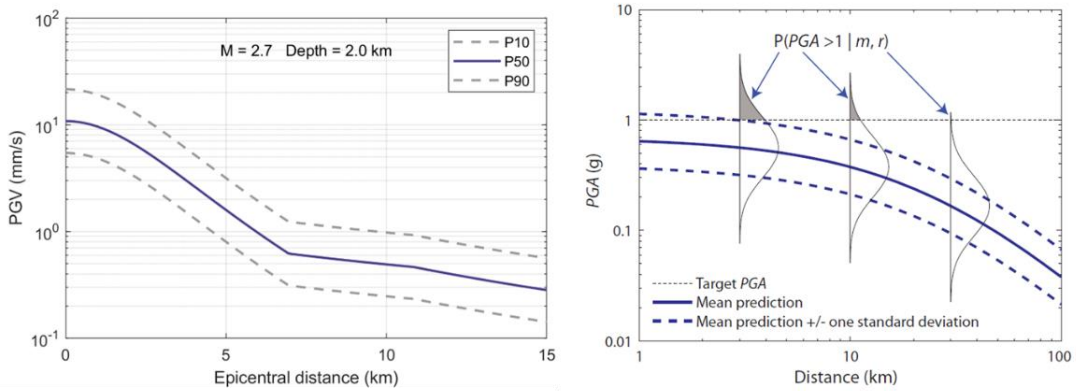

Figure 10 a) Example of PGV values with epicentral distance, for the BMR2 models and a M_L 2.7 event at 2.0 km depth. b) Example of pdfs of PGA at several distances, which are important to account for when deriving probability of exceedance values (From: Baker et al., 2021).

2.7.4 Peak ground velocity: implementation in SDRA Geothermie

For each model iteration, the largest credible earthquake magnitude value is computed. This value is used to compute the PGV distribution at various epicentral distances. To compute PGVs it is assumed that the moment magnitude is equal to the local magnitude, which is the magnitude format on which the BMR2 GMPEs were based.

It is important to consider the full probability distribution of all model realizations when considering probability of exceedance values (Figure 10). Each realization, transformed to PGV distribution, is assumed to be equally likely. These pdfs are added and normalized to yield the total probability density function of all model realizations (Figure 11a) at each epicentral distance. The pdf is converted to a probability of exceedance curve (Figure 11b). From this curve, various percentiles can be obtained, e.g., the mean value as shown in Figure 11b. In addition, the probability of exceeding a certain threshold value can be obtained. In the SHRA geothermal a threshold value of 3 mm/s is used. This value is based on the 5 mm/s which is stated in the Dutch SBR-guidelines as the characteristic threshold value of first grade damage DS1 to masonry structures (SBRCURnet, 2017). This threshold is interpreted as a 1% probability of damage. An extra safety factor for vibration-sensitive buildings leads to the 3 mm/s threshold used in the SHRA geothermal (see Mijnlieff et al., 2023). For the example shown in Figure 11, the corresponding probability of exceeding 3 mm/s at the epicenter is 0.66. Note that also the realizations are taken into account which did not lead to fault reactivation in

SRIMA – i.e., did not generate a magnitude at all. For these cases, there is zero effect on the PGV aggregate. In the example in Figure 11 in 1 out of the 15 realizations did not return a magnitude. This is visible in the plateau at the low end of PGV values in Figure 11b; the cdf of the mean values does not run to 1 but plateaus at the fraction of realization which have returned a magnitude (here: 14/15).

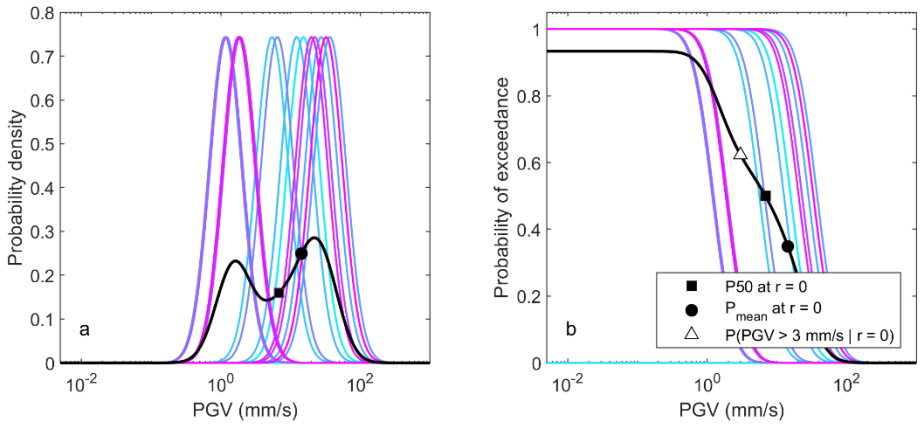

Figure 11 Synthetic example PGV distributions at the epicenter (r = 0), for 15 random magnitudes between 1.5 and 3.5 at 2.5 km depth. In 1 of the 15 cases, it is modelled that no seismicity has occurred. a) Probability density functions of individual magnitude realizations (coloured) and combined pdf of all model realizations (black). b) Probability of exceedance curves for all magnitude realizations (coloured) and combined curve (black).

From the summed pdf distributions, contours for a certain PGV threshold can be determined. In the example below, P10, and mean values for the contour of a PGV of 3 mm/s are shown (Figure 12). Respective epicentral distances are 7.52 and 4.79 km. The P90 does not exist, as the probability of exceeding 3 mm/s is 0.63 in this example, smaller than 0.90.

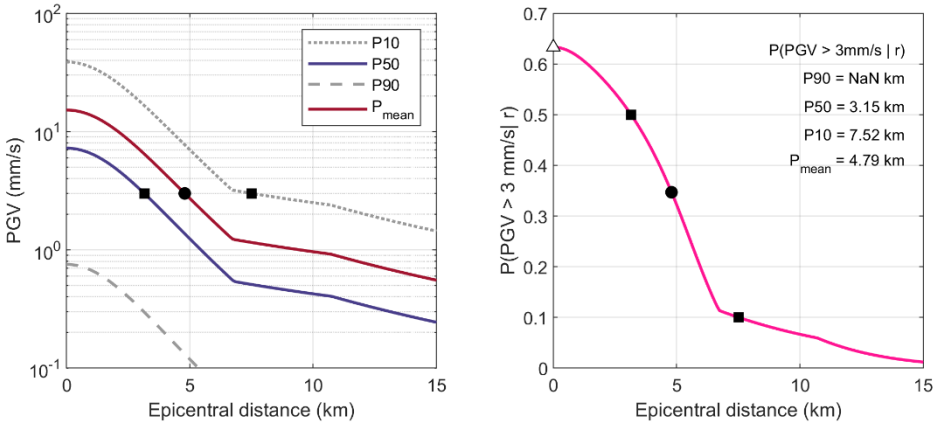

Figure 12 Contours of 3 mm/s for the same randomly picked magnitudes between 1.5 and 3.5 as shown in Figure 11. a) Contour distances of 3 mm/s shown in PGV – epicentral distance plot, for P10, P50, the mean PGV and P90 values. b) Probability of exceedance curve for 3 mm/s with epicentral distance, with P10, P50, the mean PGV, and P90 values.

The seismic hazard is determined by the probability of exceedance of the summed PGV pdfs as a function of epicentral distance, for all model iterations, conditional a cut-off value. If the mean probability of exceedance of the PGV at the epicenter is smaller than the cut-off value, no building damage is expected. The cut-off value used as damage contour is the mean probability of exceeding 3 mm/s at a certain epicentral distance. For epicentral distances greater than the 3 mm/s contour, the mean PGV is smaller than the PGV threshold and no damage probability is calculated. Within the 3 mm/s PGV contour the probability of building damage (building year pre-1940 and post-1940) is determined using fragility curves of EMS damage grade 1 (DS1) for unreinforced masonry (URM) buildings (Grunthal et al., 1998). The empirical fragility functions for DS1 have been developed by Crowley et al. (2019) using damage data from earthquakes in the Groningen field, an updated field-specific ground-motion prediction equation for PGV, that is valid for the magnitude range $1.8 \leq M_L < 4.0$ (Bommer et al., 2017), and the median PGV associated with each group of damaged buildings. Each fragility curve is defined as a lognormal function with a median value of the hazard parameter (in this case PGV) that corresponds to the threshold of the damage state and by the variability associated with that damage state. The conditional probability of exceeding DS1 given the PGV is then given by (Crowley et al., 2019):

$$P_{e\,DS1} = \boldsymbol{\Phi}\left(\frac{\ln(PGV) - \ln(\theta)}{\beta}\right) \quad 27$$

where θ is the median of PGV at which the threshold of damage state DS1 is reached, β is the standard deviation of the natural logarithm of PGV for DS1 and $\boldsymbol{\Phi}$ is the standard normal cumulative distribution function. The standard normal distribution function Φ is related to the error function:

$$\Phi = \frac{1}{2}\left[1 + \mathrm{erf}\left(\frac{\ln(PGV) - \ln(\theta)}{\sqrt{2}\,\beta}\right)\right] \quad 28$$

The DS1 fragility functions have been fitted for each of the typologies defined in the TNO (2009) study using maximum likelihood estimation, leading to the values shown in Table 3.

Table 3 Median PGV (θ) and dispersion values (β) of the updated lognormal fragility functions for DS1 (after Crowley et al., 2019).

Building category	θ (mm/s)	β
Low-rise housing < 1940	56.1	1.25
Low-rise housing ≥ 1940	113.9	1.42

The probability of exceeding the DS1 damage state is dependent on the epicentral distance: the exceedance probability declines with increasing epicentral distance. For practical reasons the probability of exceeding the DS1 damage state is aggregated to an (area-weighted) average exceedance probability applicable to the area within the defined 3 mm/s contour. This allows the user to make an inventory of the pre- and post-1940 unreinforced masonry building stock within the 3 mm/s contour and estimate the expected number of buildings exceeding the DS1 state, assuming an evenly distributed building stock over the area.

2.7.5 Comparison to PSHA and implications for hazard

The SHRA calculation as presented in this chapter consists of a scenario-based assessment of M_{LCE} and a computation of the resulting PGV and damage, summarized in

Table 1. Such a workflow leans towards what a so-called Deterministic Seismic Hazard Analysis. Deterministic hazard analysis (DSHA) is used for e.g. specific constructions (dikes, nuclear facilities, hospitals, etc.) in areas where the seismicity rates are low, or monitoring data of the earthquake distribution is absent, and when it is of importance if a structure can withstand a certain earthquake size (see Bommer 2002 for a summary). In a deterministic seismic hazard assessment the magnitude is often based on expert judgement of available information regarding the earthquake source. The largest credible earthquake magnitude M_{LCE} is then used to compute ground motions through ground motion prediction equations (GMPEs). A certain measure of these ground motions is then used to express seismic hazard, though this is not specified per time interval. In a probabilistic seismic hazard analysis (PSHA), on the other hand, ground motions are computed with an annual probability of exceedance. An example is the PSHA for the Groningen field (Bourne & Oates, 2017; Dost, Ruigrok, & Spetzler, 2017; TNO, 2020). The main characteristics of PSHA are (Figure 13):

- The full earthquake catalog is considered with rates for each magnitude – i.e. a Gutenberg-Richter distribution
- A truncation model of the catalog is often included to constrain the upper ends of the Gutenberg-Richter distribution. A maximum magnitude M_{max} (or a distribution of maximum magnitudes) is defined. In this formulation, the maximum magnitude itself will never occur with any return period; it is defined as the smallest possible magnitude that will never occur.
- All uncertainties are propagated.
- Hazard from multiple sources is aggregated.

In the article of Bommer (2002), it is argued that the difference between DHSA and PSHA may not be that sharp, as implicitly in DSHA a measure of time is present (i.e. the M_{LCE} is assumed to occur once over a projects lifetime. For a similar M_{LCE} or $M_{max,}$ both approaches will however give a very different PGV distribution and damage assessment. Whereas in DSHA the M_{LCE} fully drives the hazard, in a PSHA it will typically be the smaller-sized earthquakes that will drive the seismic hazard, since the annual rate of smaller earthquakes is much higher than that of the magnitudes approaching the maximum magnitude.

For the current SDRA Geothermie a scenario-based computation of M_{LCE} has been adopted, as observational data required to inform a seismicity catalog at the location of geothermal sites in the Netherlands are lacking. A larger degree of uncertainty is included here than in a more 'conventional' DSHA, as a range of M_{LCE} is computed and uncertainty in the PGV is accounted for. The largest difference with a PSHA remains that earthquake rates are not considered. An activity rate could have been assumed, but this would have been an arbitrary choice, without any data to substantiate it; hence the use of the scenario-based approach. This does imply that the effect of smaller-sized earthquakes on hazard and damage is not accounted for. This can have large effects because these smaller earthquakes are likely to occur more often than events with magnitudes close to the largest credible earthquake. Rigorous thought on the feasibility of implementing an SHRA for induced seismicity projects where no seismicity data is available is recommended for the coming years. If sufficient frequency-magnitude data does become available in the future, the current analysis could be adjusted to incorporate earthquake rates.

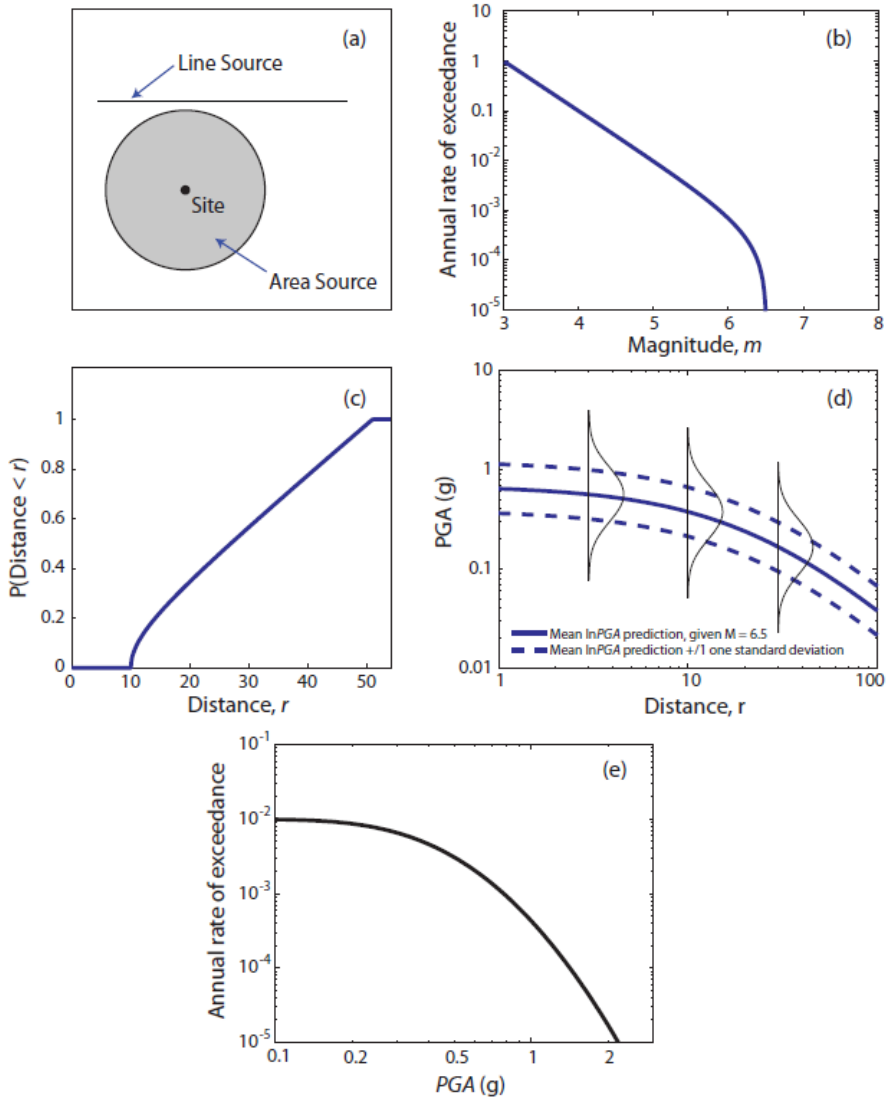

Figure 13 Typical PSHA workflow, Baker et al. (2021).

3 Concluding Remarks

This report summarizes the technical background of SRIMA (Seal and Reservoir Integrity through Mechanical Analysis). The SRIMA tool is used in the Standard extended Seismic Hazard Analysis (Standaard uitgebreide SDRA), which is part of the seismic hazard and risk assessment for geothermal projects in the Netherlands (Mijnlieff et al., 2023). SRIMA provides a scenario-based estimate of seismic hazard, by computing pressure and temperature changes around an injection well, computing stress changes on a fault at certain distance from the well, and computing the reactivated fault area, the maximum credible earthquake magnitude, the resulting PGV distribution and the damage. The calculated stress changes, in combination with the background stresses and rock properties, can also be employed to assess the probability of tensile fractures in the formations above and below the target inject formation.

An important feature of SRIMA is its probabilistic approach. This enables to make safety estimates for, e.g. the probability of breaching the seal by fracturing, and to underpin operational decisions with regard to injection. In addition, the dependence of the outcome on the input parameters can be used to steer operational choices and data acquisition investments. The probabilistic framework of SRIMA precludes the use of a complex numerical methodology. The developed tooling must be fast enough to be able to assess the effect of parameter uncertainty. SRIMA can perform at least several 100's of simulations within a few hours on a conventional laptop. Necessarily, various assumptions lie at the basis of the SRIMA tool (e.g. radial symmetry, steady-state injection), and there are aspects that cannot be included, such as strongly heterogeneous formations, complex reservoir geometries, fault slip, and (dynamic) fault weakening. Still, first order aspects of the stress changes and the dimensionality of the problem (i.e. the cooled and pressurized reservoir volume) are captured.

The risk of hydraulic fracturing is approached through an assessment of the pressure with regard to the calculated in-situ stress, with the input possibility of an excess fracturing pressure. If the pressure in the injection layer is larger than the sum of the minimum in-situ stress and the excess fracturing pressure, a hydraulic fracture is assumed to develop. When a fracture develops into the seal or base above or below the reservoir, the pressure with which the in-situ stress plus excess pressure is compared is the pore pressure in the reservoir corrected for the hydraulic head between the two depths. This is because the pressure in a potential hydraulic fracture will be controlled by the pressure at the point of injection. An estimate can thus be obtained for the maximum height of penetration of a hydraulic fracture into seal or base: it is the maximum height to which this pressure is larger than the local minimum in-situ stress. An ensemble of probabilistic runs is deployed to assess the probability of keeping the hydraulic fractures within an extent that is considered safe, and to correlate that to operational parameters like the injection pressure.

For the seismic hazard the stress changes are converted to magnitude by considering the fault area over which reactivation occurs at the end of a project's lifetime, and computing the average stress drop over that area. The translation of stress changes to magnitude is deemed conservative, under the assumption of a low background stress environment: the entire reactivated area is assumed to slip in one event, and all slip is assumed to be seismic slip (in contrast to aseismic deformation). For this reason, the computed magnitude is named the largest credible earthquake magnitude M_{LCE}. An ensemble of M_{LCE} is computed to address the

uncertainty of the input parameters. Note that due to the logarithmic dependence of magnitude on moment, the dimension of the problem (i.e. the footprint of the geothermal injection, which is typically on a scale of 100 – 1000 m) has a dominant effect on the computed M_{LCE} in case reactivation occurs. This ensemble is then converted to an aggregated PGV exceedance curve, taking into account uncertainties in the GMPE (Ruigrok & Dost, 2020). This is somewhat analogous to a Deterministic Seismic Hazard Analysis. The main differences with a probabilistic hazard analysis (PSHA) are that PSHA employs the full earthquake catalog, all uncertainties are aggregated throughout the analysis, and hazard is given in rates of exceedance per unit time (e.g. annual rate of exceedance). No event data was available to warrant a choice of activity rate in the current case, hence the scenario-based approach is presented in this report.

Assumptions have been made at all the steps of the use of SRIMA within the SHRA Geothermal, which will to a varying degree impact the computed fracturing potential and seismic hazard. These were necessary in the framework of providing in a relatively simple and fast tool for the computation of fracturing, reactivation, magnitudes and hazard, and also in the framework of having no event data available to populate e.g. seismicity rates. In the following section, several recommendations are listed for improvements that can be made in the coming years.

3.1 Recommendations

Within the current philosophy some improvements to the tool are possible. One is the incorporation of strictly non-permeable seal or base, so-called undrained conditions. Pressure changes then result from thermal expansion or contraction, and from volume strains induced by thermo-elastic and poro-elastic stress changes. Further, the output of the tool is now restricted to values on a vertical line at the well location or to values on a predefined fault. The semi-analytic tool allows calculation of pressures, temperatures and stresses at any location. Adding the possibility of providing output at carefully chosen locations, like a vertical plane through the wellbore, could considerably enhance the educational value of SRIMA and help the user to develop insight in the phenomena at hand. Finally, the tool is now restricted to radial symmetries and hence does not address faults with an offset. In a first analysis, it was shown under which conditions this assumption was still valid. An important improvement would be to evaluate the effect of fault throw under a wider range of conditions using both 2D and 3D solutions (e.g. obtained from Finite Element modeling), and based on such an analysis to develop proxy models that mimic the effect of such faults to the further symmetrical SRIMA geometry.

The hydraulic fracturing calculation is limited. There is neither a fracture propagation module nor an influence of the presence of the fracture on the stress field. The code merely provides a sensible estimate of a possible extent of hydraulic fracture growth. When SRIMA indicates a large risk of considerable fracture propagation, the use of a dedicated hydraulic fracturing software is warranted.

To compute the M_{LCE} various assumption have been made. Is was assumed that the entire reactivated area (SCU >1) participates in one big slip event at the end of the project lifetime. In reality, stress build-up on a fault in the cooled reservoir volume is likely gradual, and hence fault reactivation is expected to be a gradual process with multiple events occurring each time the critical conditions for earthquake instability (e.g. Uenishi & Rice, 2003) are met. Future implementations could address this by modeling fault slip, though this may still be beyond the scope of a simplified tool as SRIMA. It is also assumed that all of the estimated slip of that

event is seismic. In reality part of the fault slip may occur aseismically. Improved understanding through lab measurements and field monitoring in the future may help to constrain the (play- or lithology-specific) seismic/aseismic slip partitioning on faults near geothermal injection wells. Such a partitioning factor could be included to scale the M_{LCE}.

To compute hazard, the M_{LCE} was used but earthquake rates were not included as at the moment no (micro)seismic observational data is available near geothermal projects. On the other hand, for the hazard and damage calculation, implicitly it is assumed M_{LCE} occurs once over a project's lifetime, and hence earthquake rate is implicitly present. The resulting hazard is however different from taking into account the full earthquake catalog and rates as is done in PSHA. Whereas in the current approach M_{LCE} drives hazard, in a PSHA approach the smaller-sized earthquakes dominate the hazard as these occur more often than the largest credible event. For the coming years, it is recommended to evaluate the applicability of the approach to the geothermal sites in the Netherlands and to update the SHRA approach as more (microseismic) data becomes available. This could be seismicity rates linked to operations, but also observational data regarding the stress drop and the aforementioned reservoir-specific partitioning between seismic and aseismic deformation.

To compute damage, PGV is used as a proxy for the initiation of damage to buildings. The chosen cut-off value of PGV to take into account is inspired by the existing SBR-A guideline. The SBR-A guideline defines vibration threshold criteria to which measurements at the building structure are compared. Replacing (deterministic) measurements with vibrations predicted by (probabilistic) models in relation to the SBR-A is not in all cases trivial. First, to better align ground motion prediction model to the SBR-A guidelines, the vertical component of the ground velocity should be taken into account. This is especially the case for epicentral distances smaller than 2 km. An update of the current BMR2 PGV model including the vertical velocity component is therefore recommended. Second, the SBR-A guideline is developed for vibrations mainly due to construction work and rail- and road traffic. Earthquakes are not mentioned as a source, but can be categorized using the SBR-A. Because the earthquake wavefield differs in essence from the types of vibrations it is recommended to evaluate (and possibly adapt) the guidelines' safety factors in case of earthquake loading. Third, it is recommended to compute building fragility functions due to earthquake loading to investigate if the PGV threshold values in the SBR-A can be maintained in case of earthquake loading.

4 References

- Aki, K. (1966). Generation and propagation of G waves from the niigate earthquake of june 16, 1964. part 2. estimation of earthquake moment, released energy, and stress-strain drop from the G wave spectrum. Bulletin of the Earthquake Research Institute, 44, 73-88.
- Baker, J. W., Bradley, B. A., and Stafford, P. J. (2021). Seismic Hazard and Risk Analysis. Cambridge University Press, Cambridge, England.
- Bakx, E., Buijze, L., & Wassing, B. B. T. (2022). Formation, lithology and region-specific stress field in the Netherlands. (Draft Report). Utrecht: TNO. . (Report prepared within the WarmingUp project Theme 4B).
- Barends, F. (2010). Complete solution for transient heat transport in porous media, following Lauwerier's concept. Paper presented at the SPE Annual Technical Conference and Exhibition.
- Bommer, J.J. (2002). Deterministic vs. probabilistic seismic hazard assessment: An exaggerated and obstructive dichotomy. Journal of Earthquake Engineering, Vol. 6, p 43-73.
- Bommer, J. J., Stafford, P.J. & Ntinalexis M. (2017). Emperical Ground-Motion Prediction Equations for peak ground velocity from small-magnitude earthquakes in the Groningen field using multiple definitions of the horizontal component of motion, NAM Platform, November 2017.
- Bommer, J. J., Stafford, P.J. & Ntinalexis, M. (2019). Updated emperical GMPEs for PGV from Groningen earthquakes — March 2019, NAM Study Report.
- Bourne, S. J., & Oates, S. J. (2017). Extreme threshold failures within a heterogeneous elastic thin sheet and the spatial-temporal development of induced seismicity within the groningen gas field. Journal of Geophysical Research: Solid Earth, 122(12), 10,299-10,320. doi:10.1002/2017JB014356.
- Buijze, L., Van den Bogert, P., Wassing, B. B. T., & Orlic, B. (2019). Nucleation and arrest of dynamic rupture induced by reservoir depletion. Journal of Geophysical Research: Solid Earth, 124(4), 3620-3645.
- Buijze, L., Fokker, P.A. & Wassing, B. (2021). Quantification of induced seismicity potential of geothermal operations. WarmingUP, 060.43190.
- Candela, T., Van der Veer, E. F., & Fokker, P. A. (2018). On the Importance of Thermo-elastic stressing in Injection-induced earthquakes. Rock Mechanics and Rock Engineering, 51(12), 3925-3936. doi:https://doi.org/10.1007/s00603-018-1619-6.
- Carslaw, H. S., & Jaeger, J. C. (1992). Conduction of heat in solids Clarendon press.
- Cowley, H., Pinho, R. & Uilenreef, J. (2019). Probabilistic damage assessment of buildings due to induced seismicity. Bulletin of Earthquake Engineering 17:4495-4516. Doi:https://doi.org/10.1007/s10518-018-0462-1.
- Dake, L. P. (1983). Fundamentals of reservoir engineering, Elsevier.
- Dost, B., Edwards, B., & Bommer, J. (2016). Local and moment magnitudes in the groningen field. (Scientific Report). Assen: NAM.

- Dost, B., Ruigrok, E., & Spetzler, J. (2017). Development of seismicity and probabilistic hazard assessment for the groningen gas field. Netherlands Journal of Geosciences, 96(5), s235-s245.
- Fjaer, E., Holt, R. M., Horsrud, P., Raaen, A. M., & Risnes, R. (2008). Petroleum related rock mechanics (2nd Edition ed.) Elsevier.
- Fokker, P.A., Buijze, L, & Wassing, B.B.T. (2023) A semi-analytical model for poro-thermoelastic stresses by injection in a finite-height layer. Presented at the 57th US Rock Mechanics / Geomechanics Symposium, Atlanta GA (USA), 25-28 June 2023.
- Geertsma, J. (1957). A remark on the analogy between thermoelasticity and the elasticity of saturated porous media. Journal of the Mechanics and Physics of Solids, 6(1), 13-16.
- Geertsma, J. (1973). Land subsidence above compacting oil and gas reservoirs. Journal of Petroleum Technology, (June), 734.
- Grant, M. (2013). Geothermal reservoir engineering Elsevier.
- Grunthal, G., Musson, R.M.W., Schwarz, J. & Stucci, M. (1998). European Macroseismic Scale 1998. Centre Europeen de Geodynamique et de Seismologie, ISBN No2-87977-008-4.
- Hanks, T. C., & Kanamori, H. (1979). A moment magnitude scale. Journal of Geophysical Research, 84(85), 2348-2350.
- Hutka, G., Cacace, M., Hofmann, H., Mathur, B., & Zang, A. (2023). Investigating seismicity rates with Coulomb failure stress models caused by pore pressure and thermal stress from operating a well doublet in a generic geothermal reservoir in the Netherlands. Netherlands Journal of Geosciences, 102, E8. doi:10.1017/njg.2023.7
- Jansen, J., Singhal, P., & Vossepoel, F. (2019). Insights from closed-form expressions for injection-and production-induced stresses in displaced faults. Journal of Geophysical Research: Solid Earth, 124 (7), 7193-7212.
- Kanamori, H., & Anderson, D. L. (1975). Theoretical basis of some empirical relations in seismology. Bulletin of the Seismological Society of America, 65(5), 1073.
- Kirsch, C. (1898). Die theorie der elastizitat und die bedurfnisse der festigkeitslehre. Zeitschrift Des Vereines Deutscher Ingenieure, 42, 797-807.
- Kivi, I. R., Pujades, E., Rutqvist, J., & Vilarrasa, V. (2022). Cooling-induced reactivation of distant faults during long-term geothermal energy production in hot sedimentary aquifers. Scientific reports, 12(1), 2065.
- Mijnlieff, H., De Vries, S., Jaarsma, B., Vogelaar, B. (2023). Seismische Dreigings- en Risicoanalyse voor aardwarmteprojecten in Nederland (English: Seismic Hazard and Risk Assessment for geothermal projects in The Netherlands).
- Mossop, A. (2001). Injection Induced Seismicity: A Thermoelastic Model, Ph.D. thesis, chapter 5, Stanford University.
- Mulders, F. M. M. (2003). Modelling of stress development and fault slip in and around a producing gas reservoir. (Doctoral Thesis, Technical University of Delft).
- Myklestad, N. O. (1942). Two problems of thermal stress in the infinite solid. Journal of Applied Mechanics, , A-136-A-143.
- Nield, D. A., & Bejan, A. (2006). Convection in porous media Springer.
- Orlic, B., & Wassing, B. B. T. (2013). A Study of Stress Change and Fault Slip in Producing Gas Reservoirs Overlain by Elastic and Viscoelastic Caprocks. Rock Mechanics and Rock Engineering, 46 (3), 421-435.

- Perkins, T. K., & Gonzalez, J. A. (1985). The effect of thermoelastic stresses on injection well fracturing. Society of Petroleum Engineers Journal, 25(1), 78-88. doi:https://doi.org/10.2118/11332-PA.
- Ruigrok & Dost (2022). Advice on the computation of peak-ground-velocity confidence regions for events in gas fields other than the Groningen gas field. Technical report: TR-386.
- SBRCURnet, 2017. SBR Trillingsrichtlijn A: Schade aan bouwwerken: 2017, 91p.
- SodM. (2016). Methodiek voor risicoanalyse omtrent geïnduceerde bevingen voor gaswining - tijdelijke leidraad voor adressering MBB. (No. VERSIE 1.2). Den Haag: State Supervision of Mines.
- Starr, A. T. (1928). Slip in a crystal and rupture in a solid due to shear. Mathematical Proceedings of the Cambridge Philosophical Society, 24(04), 489-500.
- TNO (2009). Kalibratiestudie schade door aardbevingen. TNO-034-DTM-2009-04435.
- TNO. (2020). Probabilistic seismic hazard and risk analysis in the TNO model chain Groningen. (No. TNO2020 R11052). Utrecht, the Netherlands: TNO. doi:https://kempro-gramma.nl/file/download/57979610/tno2020-r11052-wvd-pshra-tno-model-chain-groningen-gelakt.pdf.
- Uenishi, K., & Rice, J. R. (2003). Universal nucleation length for slip-weakening rupture instability under nonuniform fault loading. Journal of Geophysical Research: Solid Earth, 108(B1).
- Van den Bogert, P. A. J. (2015). Impact of various modelling options on the onset of fault slip and fault slip response using 2-dimensional Finite-Element modelling. Restricted , Report No. SR.15.11455, Rijswijk: Shell Global Solutions International B.V.
- Wang, Y., & Dusseault, M. B. (2003). A coupled conductive–convective thermo-poroelastic solution and implications for wellbore stability. Journal of Petroleum Science and Engineering, 38(3-4), 187-198.

A.1 Validation of SRIMA

In SRIMA a number of assumptions have been made regarding the reservoir geometry, the pressure and temperature distributions, and the poro- and thermo-elastic stress computation. In the following we report our benchmark of SRIMA against other software packages. The goal is to warrant these assumptions, assess their validity range and/or show under which conditions SRIMA remains conservative with respect to more comprehensive analyses. In this Appendix we employed a version of SRIMA that also could give output on a horizontal or vertical line, or on a vertical plane containing the well.

A.1.1 Validation of the pressure and temperature calculation in SRIMA

We have validated the SRIMA-calculated temperature and pressure fields to output generated by Eclipse for the same input parameters. To this end we modelled an aquifer in which we injected cold water for 30 years. The base case of the aquifer thickness of 100 m was varied: 30 m and 300 m thickness were also tested. Figure 14 and Figure 15 show good agreement between the SRIMA results and the Eclipse results for the temperature. For thicker and thinner reservoirs, the agreement was the same. Only some numerical diffusion in Eclipse caused a more gradual temperature decrease in the reservoir; further, the leakage of (negative) heat to the bounding layers caused some vertical differentiation of the temperature profile in the aquifer near the thermal boundary.

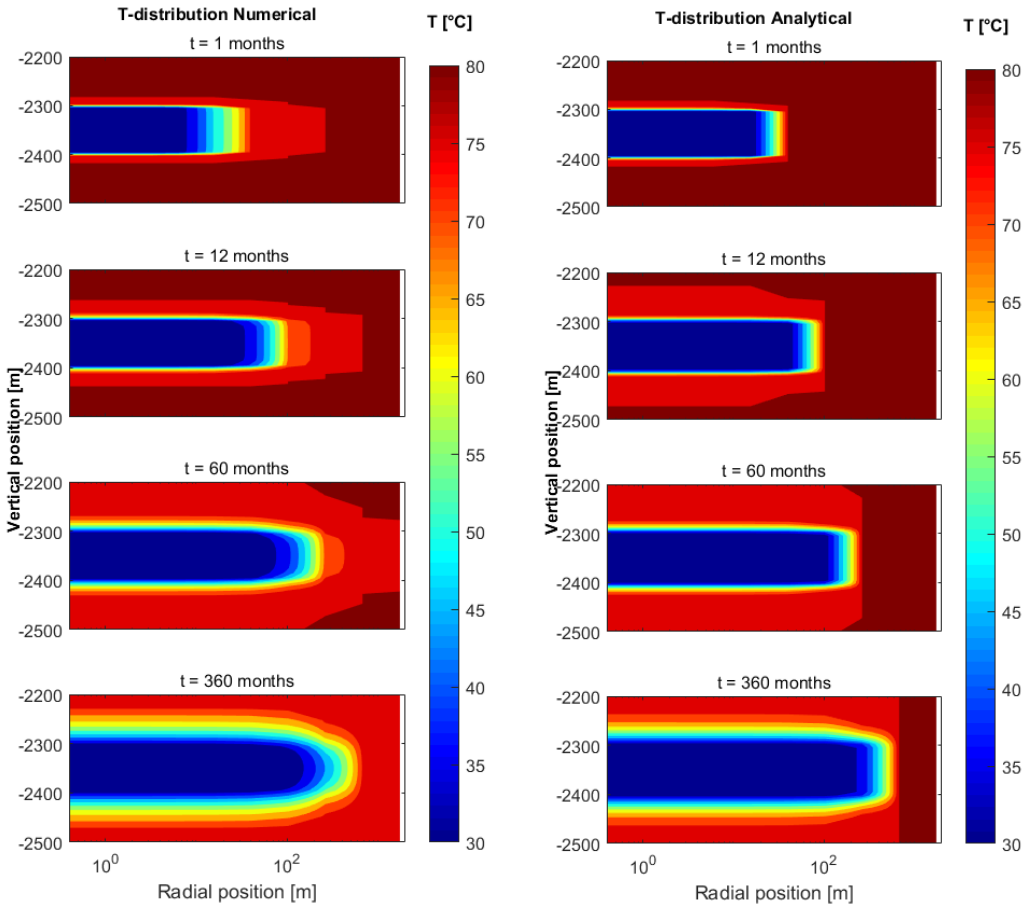

Figure 14 Contour plots of the benchmark results of the temperature correlations. Left: numerical results. Right: Analytical results with SRIMA. Note that the radial axis is spaced logarithmically

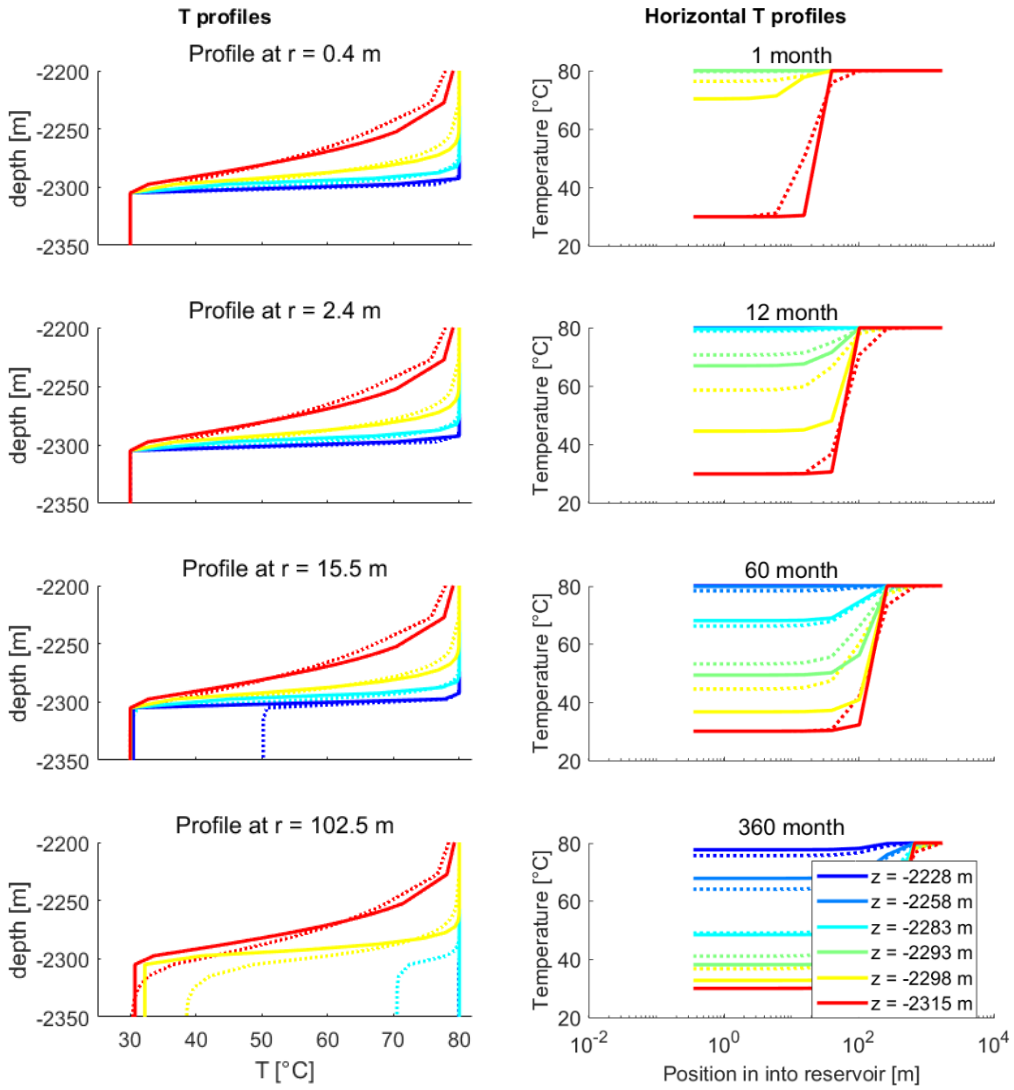

Figure 15 Line plots of the benchmark results of the temperature correlations at different distances from the well. Left: vertical profiles. Colors dark blue, light blue, yellow and red indicate timings at 1, 12, 60 and 360 months; dotted curves are numerical results and solid curves are analytical results. Right: horizontal profiles at different vertical positions and different times.

The pressure response as calculated in SRIMA was also verified using Eclipse. Figure 16 and Figure 17 give the results. As expected, the pressure profiles are indeed logarithmically decreasing with the radius, with different slopes in the cold and hot zones. This is best demonstrated in the profiles along a horizontal line: the pressures in the reservoir (red lines in right plot of Figure 17) show a change in slope at the position of the cold front. Profiles for the 30-m and 300-m thick reservoir showed essentially the same behavior. The correspondence between numerical and analytical results in the bounding layers is slightly worse than for the temperature; this is mainly due to the pressure gradient present along the complete reservoir. Actually, this validation was used as a benchmark for the optimization of the choice of the effective cylinder pressure mentioned in Section 2.2.4.

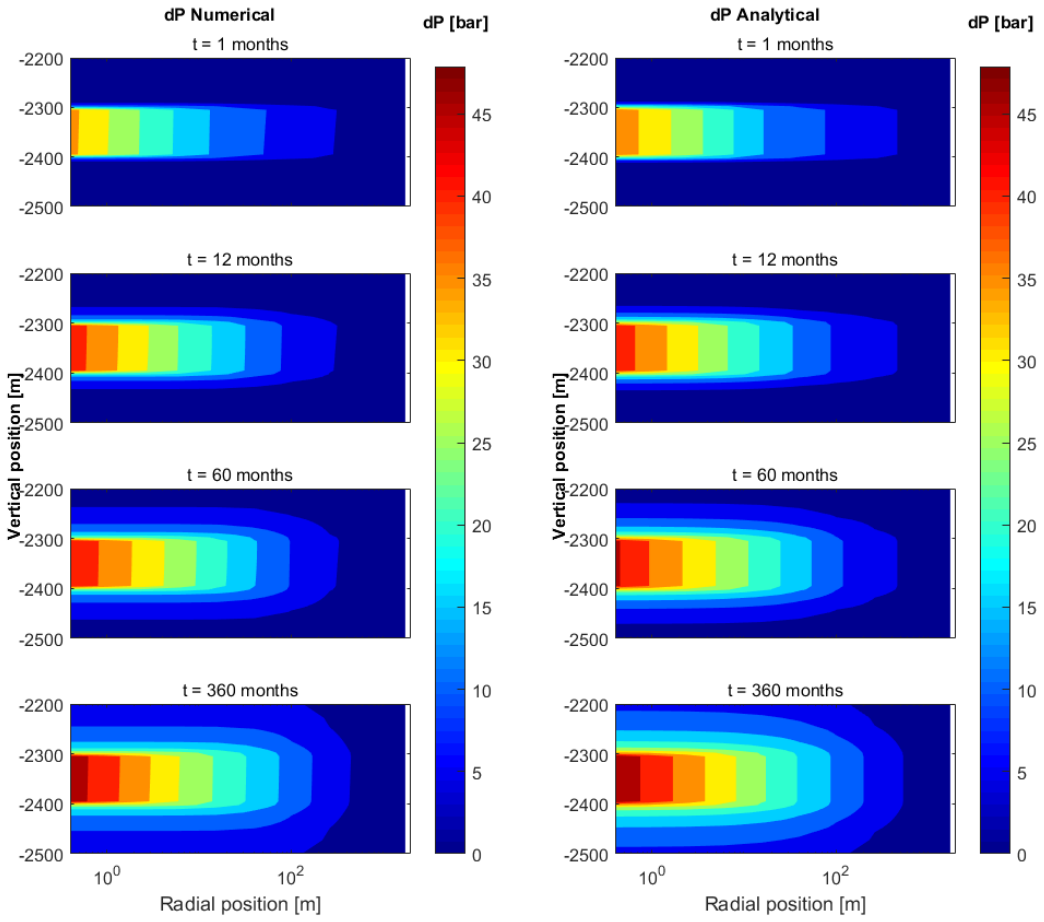

Figure 16 Contour plots of the benchmark results of the pressure correlations. Left: numerical results. Right: Analytical results with SRIMA. Note that the radial axis is spaced logarithmically.

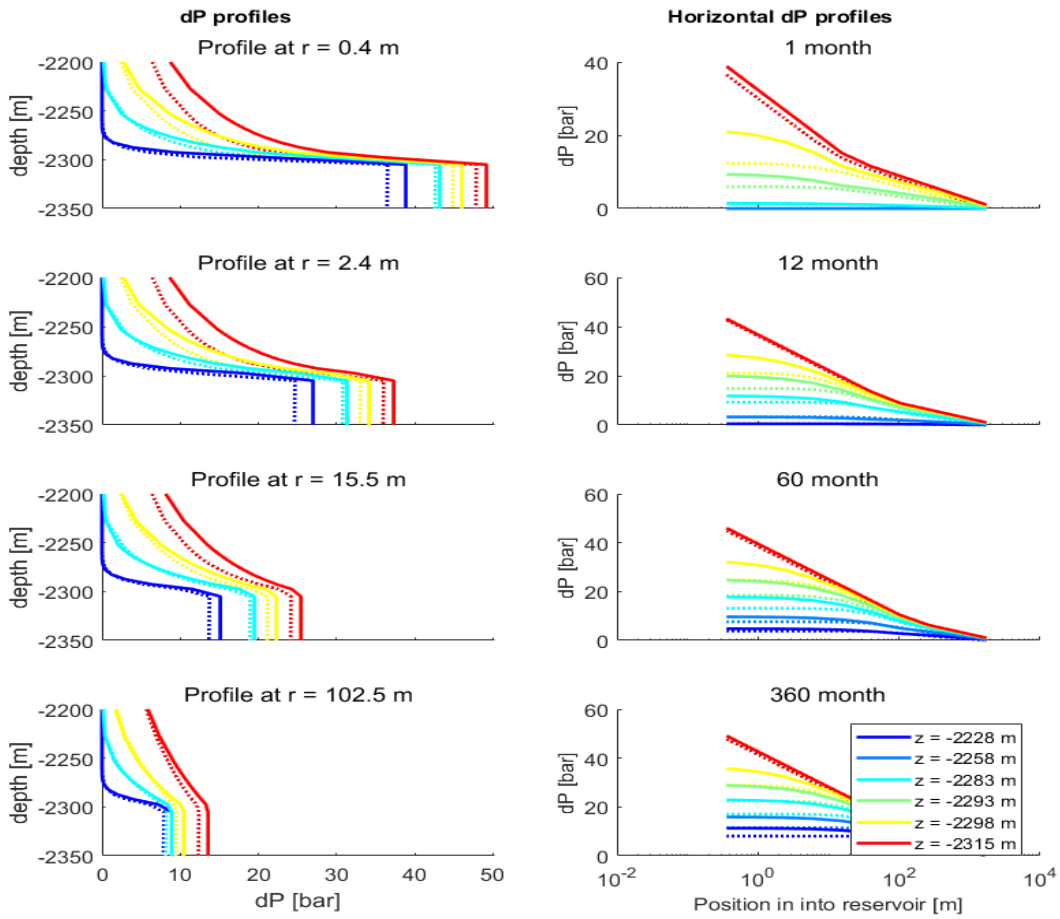

Figure 17 Line plots of the benchmark results of the pressure correlations at different distances from the well. Left: vertical profiles. Colours dark blue, light blue, yellow and red indicate timings at 1, 12, 60 and 360 months; dotted curves are numerical results and solid curves are analytical results. Right: horizontal profiles at different vertical positions and different times

A.1.2 Validation of stress calculation

A.1.2.1 Model setup and input parameters

SRIMA simulates the poro-thermo-elastic stress changes due to injection into a reservoir formation overlain by a seal formation and underlain by a base formation (Section 2.2.1). The calculation of the stress change has been benchmarked against the Finite Element software DIANA FEA. The model setup in DIANA is similar to that of SRIMA; however, whereas seal and base are assumed to have infinite height in SRIMA a free surface is included in DIANA and the model depth is finite with a maximum depth of -5000 m (Figure 18). Fixed displacement boundaries were imposed at the model sides and base, preventing displacement in the direction perpendicular to the boundary but allowing displacement parallel to the boundaries. Like in SRIMA the model width was 2500 m and the well radius 0.2 m, and the reservoir formation was situated at -2300 m with a thickness of 100 m.

The formations were modeled with linear triangular and quadrilateral elements (T6AXI and Q8AXI). The element size increased from 2 m at the well in the reservoir to a maximum of 20 m further away from the well.

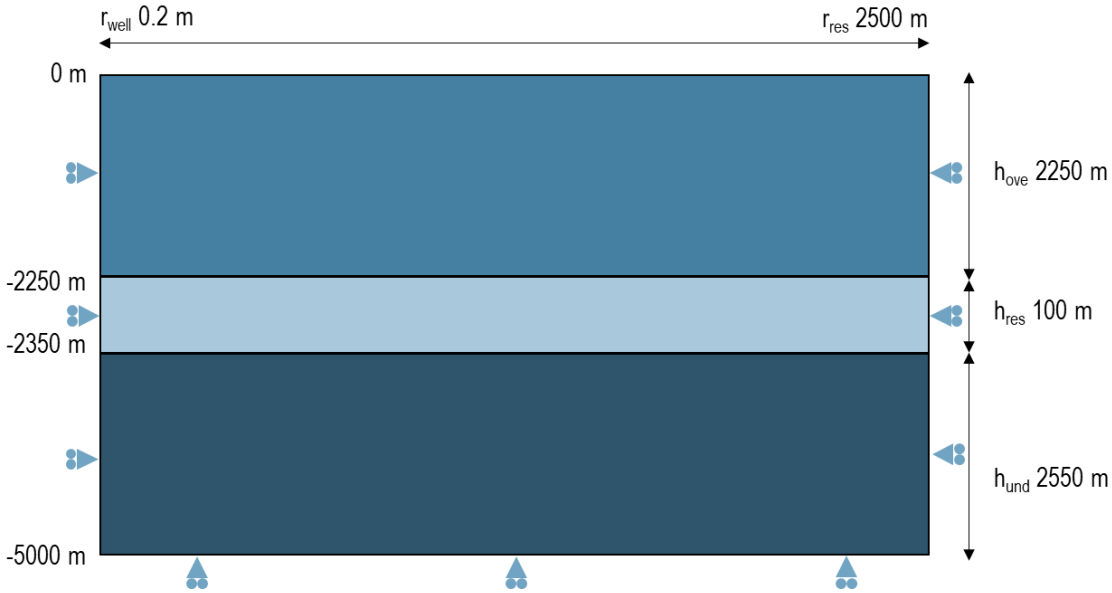

Figure 18 Axisymmetric model in DIANA used to benchmark stress calculation in SRIMA. Triangles indicate the presence of displacement boundaries preventing motion perpendicular to the boundary.

Table 1 Input parameters used for the benchmark of stress changes computed in SRIMA vs Eclipse and DIANA FEA.

Parameter (DIANA & SRIMA)	Symbol	Unit	Value
Mid depth	y_{mid}	m	2300
Reservoir thickness	h	m	100 (30, 300)
Throw	t	m	NA
Dip	θ	°	70
Vertical stress gradient	$\Delta\sigma_v/\Delta y$	MPa/km	22.6
Stress ratio σ_h / σ_v	K_0	-	0.708
Horizontal stress ratio σH / σh	σ_H / σ_h	-	1
Pressure gradient	$\Delta\sigma_v/\Delta y$	MPa/km	10.72
Strike with respect to σ_H	ϕ	deg	0
Overpressure in the reservoir	P_{exc}	MPa	0
Biot coefficient	α	-	1
Poisson's ratio	ν	-	0.1
Young's modulus	E	GPa	15 (3.75, 60)
Linear thermal expansion coefficient	η	$°C^{-1}$	$1.20 \cdot 10^{-5}$
Static friction	f_s	-	0.6
Flow-Temp parameters (Eclipse & SRIMA)			
Permeability	k	mD	500
Overburden permeability	k_{seal}	mD	$3.0 \cdot 10^{-5}$
Reservoir temperature	T_{res}	°C	80
Injection temperature	T_{inj}	°C	35
Thermal conductivity	K_{rock}	W/mK	3.50
Specific heat capacity water	c_{fluid}	J/kgK	4200
Specific heat capacity rock	c_{rock}	J/kgK	850
Seal density	ρ_{rock}	kg/m3	2200
Seal porosity	ϕ_{seal}	-	0.1
Seal Poisson ratio	ν_{seal}	-	0.1
Density water	ρ_w	kg/m3	1000
Mass injection rate	q	kg/s	50
Water viscosity at T0	μ_c	Pas	0.0003
Water viscosity at Tinj	μ_h	Pas	0.001
Total compressibility	c	1/Pa	$4.0 \cdot 10^{-10}$

For the validation of the induced stresses, pressures and temperatures were computed in SRIMA. This PT-field was used as an input in DIANA, so both SRIMA and DIANA started with the same PT-changes from which the poro-thermo-elastic stresses are computed. The PT-field was interpolated at the node locations of the DIANA mesh. The PT-field after 30 years of injection was used for the benchmark. A constant initial temperature of 80 degrees was assumed for the reservoir and seal and base formations.

In the benchmark exercise we compared both the horizontal, vertical and shear stress, as well as the Coulomb Stress Changes, which are important for fault reactivation. Coulomb Stress Changes (CSC) are calculated as

$$CSC = \Delta\tau - \mu\Delta\sigma_n' \quad (29)$$

Where Δτ is the shear stress change, $\Delta\sigma_n'$ is the effective normal stress change on the fault, and μ is the static friction coefficient. For the Coulomb Stress Change a fault dip of 70° was used and a friction coefficient of 0.6.

A.1.2.2 Stress changes – Uniform elasticity

Figure 19 shows the horizontal and vertical stress changes modeled in DIANA and SRIMA after 30 years of injection, and Figure 20 shows the Coulomb stress changes for a fault dip of 70°. The cooling front extends for 570m from the wellbore, which is clearly reflected in the stress changes; the largest stress changes occur within the cooled volume. Since the pressure changes are small the poro-elastic response is limited, and the stress response is dominated by thermo-elastic stress changes. The stress response to injection can be summarized as following:

- A decrease in total horizontal stress in the cooled volume, of 8.1 MPa for the current model. As a comparison; this is about 10% less than the horizontal stress decrease for the same amount of cooling (ΔT = -45°) for a laterally extensive reservoir, which is given by $\Delta\sigma_{x(laterally\ extensive)} = A_T\Delta T$ = -9 MPa (Figure 19), showing the effect of the limited width on the stress changes.
- A decrease in total vertical stress in the cooled volume. This decrease is much smaller than the horizontal stress decrease, with a maximum decrease of -2 MPa (Figure 19).
- The largest shear stress changes occur at the outer edges of the cooled front (Figure 19).

The Coulomb Stress Change is largest within the cooled volume (Figure 20, Figure 21). The positive values of the CSC indicate that the stress becomes more critical for the typical normal faulting orientation considered here.

Vertically oriented stress concentrations can be seen in the vertical stress changes computed in SRIMA (Figure 19, Figure 21). These stress concentrations are an artefact due to simplifications made for the analytical thermo-elastic stress calculation. The temperature field was approximated with 10 cylinders, each with a uniform temperature decrease of 10% of the total temperature decrease and a radius corresponding to 10% temperature decrease. The thermo-elastic stresses of each of these 10 cylinders can be computed analytically using the Myklestad solution, and stress changes of each cylinder are superimposed to obtain the total thermo-elastic stress changes (Section). In DIANA the thermo-elastic stress is computed directly from the temperature field and no such concentrations are seen.

Furthermore, the comparison between SRIMA and DIANA FEA shows that, for uniform elasticity:

- SRIMA overestimates the horizontal stress decrease within the cooled reservoir volume by ~7% (Figure 21).
- SRIMA underestimates the vertical stress decrease within the cooled reservoir volume with ~1 MPa which is ~30-50% of the total vertical stress decrease (Figure 19, Figure 21). In Figure 19 the variations in vertical stress due to the approximation of the temperature with discrete cylinders as mentioned above can be seen, with abrupt changes in vertical stress of ~0.5 MPa which locally cause larger differences with respect to the DIANA results.
- SRIMA overestimates the Coulomb Stress change on a fault within the cooled reservoir volume by 15%, and by up to 30% in the cooled volume of the seal or base (Figure 20, Figure 21).

SRIMA is thus conservative for fault reactivation within the cooled volume, for a normal faulting regime and relatively steep faults.

Just to the side of the cooled volume (~600 m from the well) SRIMA underestimates the vertical stress increase and horizontal stress decrease. The resulting Coulomb stress change is underestimated by SRIMA; hence, SRIMA is not conservative just outside of the cooling front.

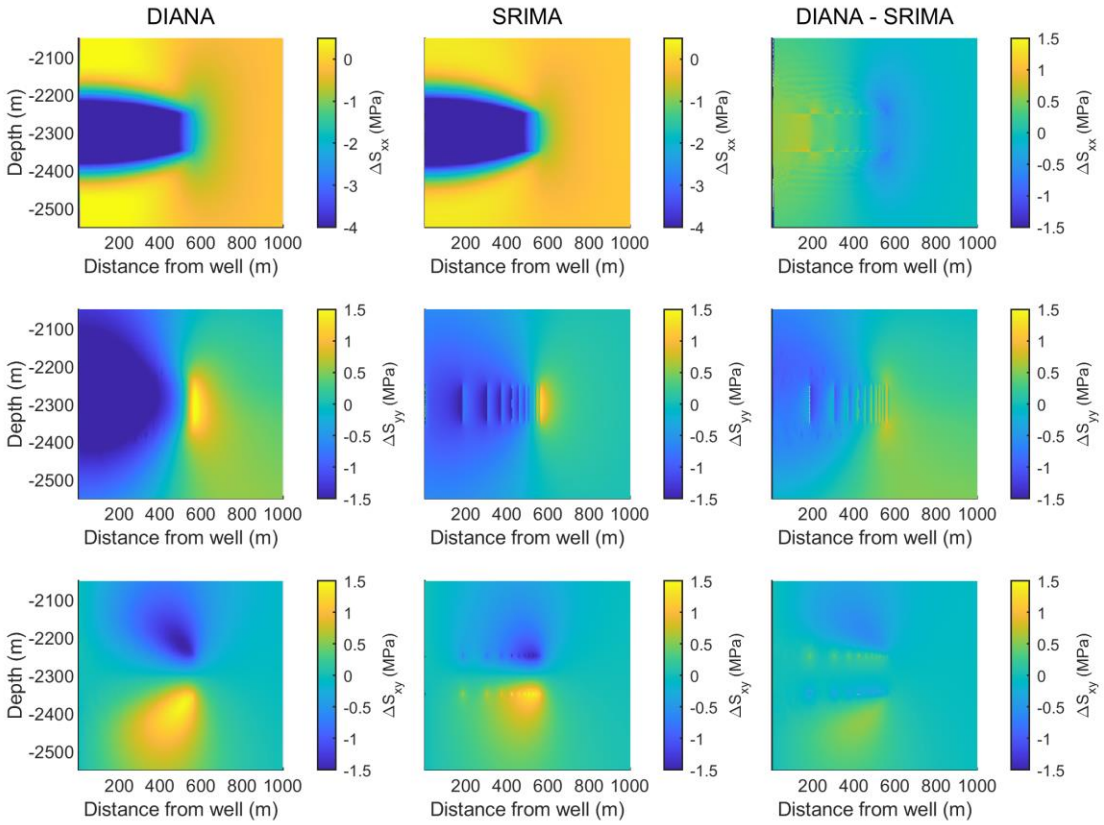

Figure 19 Stress changes modeled in DIANA and SRIMA and differences between stress changes in both models, for a uniform elastic properties. Stress changes are computed after 30 years of injection, assuming the same pressure and temperature changes for both models. Horizontal stress change: ΔS_{xx}, vertical stress change: ΔS_{yy}, and shear stress change: ΔS_{xy} in the medium. Left column shows DIANA results, and the middle column the results from SRIMA. Right column shows the difference in stress change between DIANA and SRIMA, with positive values indicating the stress computed in DIANA is larger than in SRIMA.

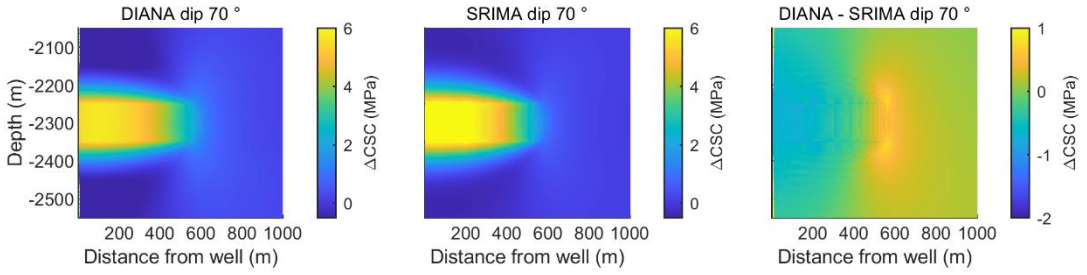

Figure 20 Coulomb Stress Changes modeled in DIANA and SRIMA and differences between stress changes in both models, for a uniform elastic properties, a dip of 70° and a friction coefficient of 0.6. Stress changes are computed after 30 years of injection.

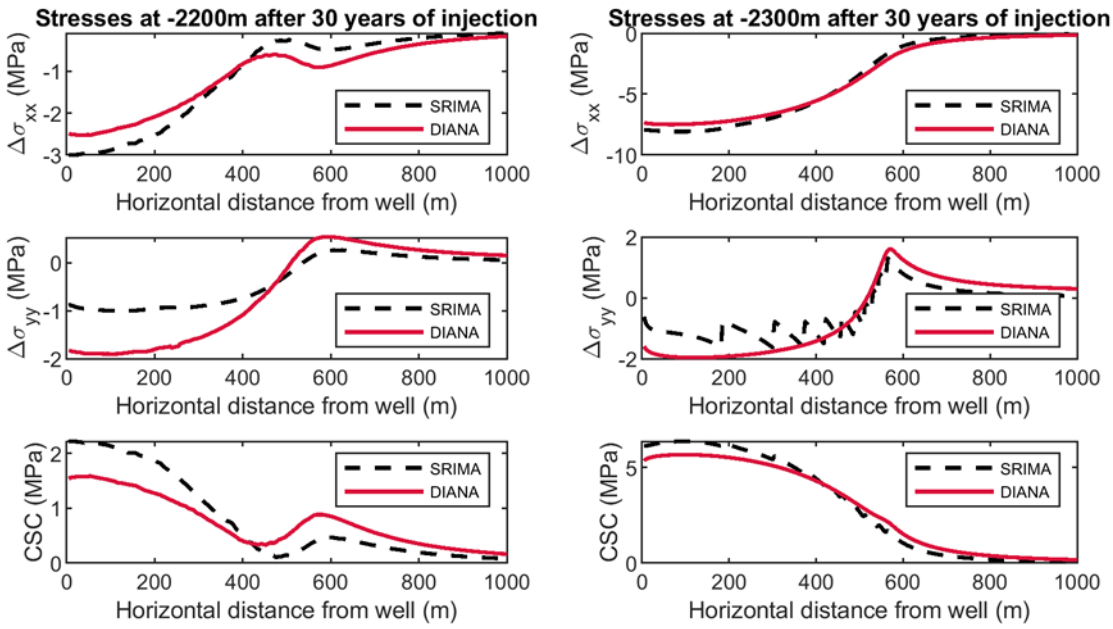

Figure 21 Comparison of horizontal and vertical stress changes and Coulomb Stress Changes computed in DIANA and SRIMA at different depths, for uniform elasticity. Lefthand side: -2200 m depth, 50 m up into the seal formation. Righthand side: -2300 m depth, in the middle of the reservoir.

A.1.2.3 Stress changes – Stiffer seal and base

The poro-thermo-elastic stress changes have also been compared for heterogeneous elasticity, with seal and base formations having a 4x higher stiffness than the reservoir (Figure 22 – Figure 24). Note that this is an upper bound to stiffness contrasts, in reality it is likely less and model differences resulting from heterogeneous elasticity are also less.

The comparison between SRIMA and DIANA FEA shows that, for a 4x stiffer seal and base formation, the largest horizontal stress decrease and Coulomb stress increase occur in the cooled parts of the seal and base formations due to the higher stiffness.

Within the reservoir the agreement between both the horizontal and vertical stress changes computed in DIANA and SRIMA is good (<5% difference), though artificial stress concentrations in vertical stress locally cause larger differences.

The agreement between the stress changes within the cooled reservoir volume is better than for uniform elasticity, likely because the stiff seal and base reduce stress arching effects, which are not captured in SRIMA.

- SRIMA overestimates the horizontal stress decrease in the cooled parts of the seal and base by ~15-20%
- SRIMA underestimates the vertical stress decrease above and below the cooled reservoir area by 50%
- The Coulomb stress changes (CSC) computed in the cooled reservoir volume show good agreement, but SRIMA overestimates the Coulomb stress change in the cooled parts of the seal and base by ~30%. Again, SRIMA is thus conservative in that it returns a larger CSC than DIANA.

- To the side of the cooled parts of the seal and base (i.e. at distance > 550 m, in the seal and base), SRIMA underestimates the Coulomb stress change. However, the rock volume over which this happens is limited to 100 – 200 m.

The discrepancies are related to the application of analytical equations developed for a homogeneous body.

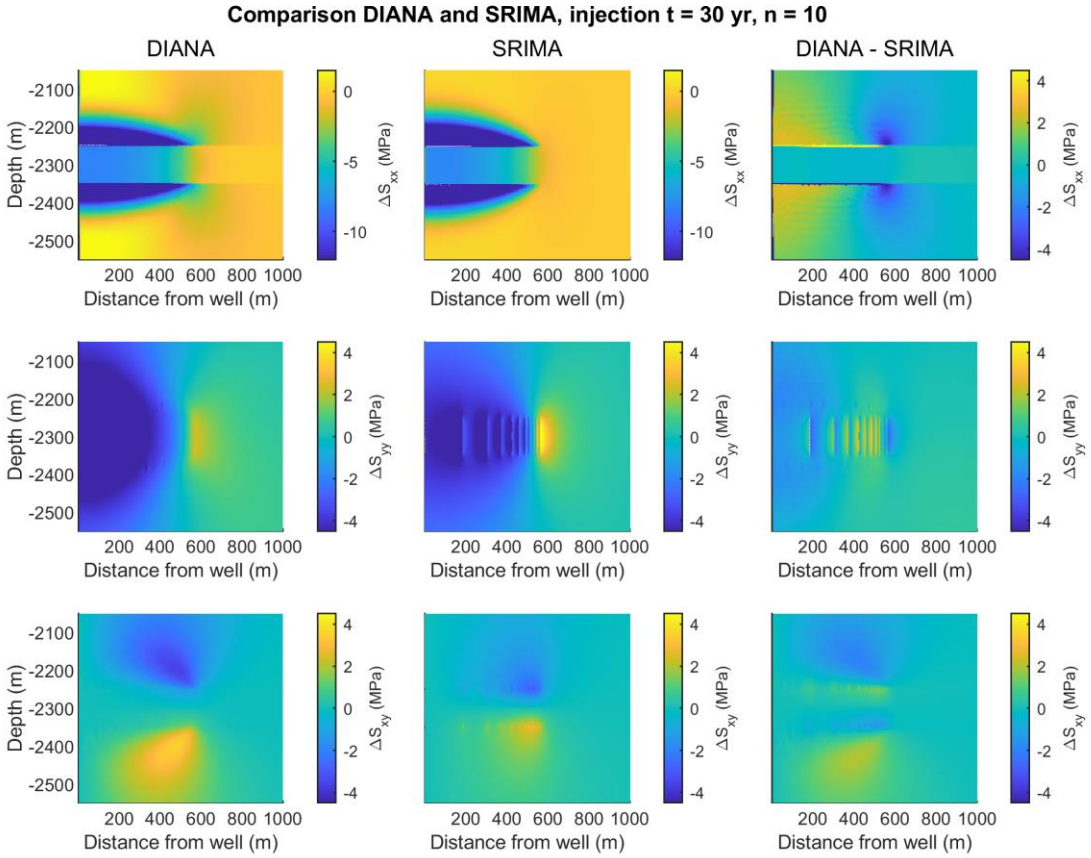

Figure 22 Stress changes modeled in DIANA and SRIMA and differences between stress changes in both models, for a 4x stiffer seal and base formation. Stress changes are computed after 30 years of injection. Horizontal stress change: ΔS_{xx}, vertical stress change: ΔS_{yy}, and shear stress change: ΔS_{xy}. Right column shows the difference in stress change between DIANA and SRIMA, with positive values indicating the stress computed in DIANA is larger than in SRIMA.

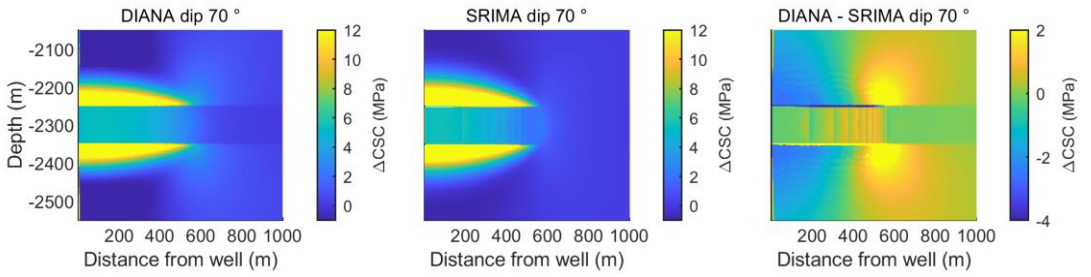

Figure 23 Coulomb stress changes modeled in DIANA and SRIMA and differences between stress changes in both models, for a 4x stiffer seal and base formation. Coulomb stress changes (ΔCSC) are computed after

30 years of injection, for a 70° dipping fault at all locations in the model domain. Right column shows the difference in stress change between DIANA and SRIMA, with positive values indicating the Coulomb stress computed in DIANA is larger than in SRIMA.

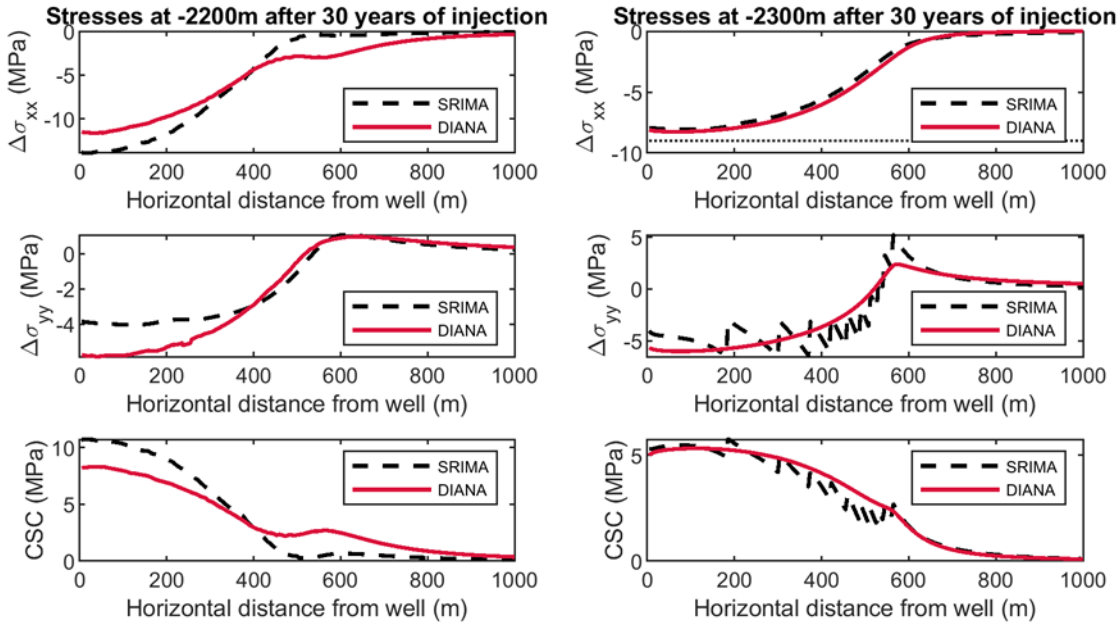

Figure 24 Comparison of horizontal and vertical stress changes and Coulomb Stress Changes computed in DIANA and SRIMA at different depths, for 4x stiffer seal and base formations. Lefthand side: -2200 m depth, 50 m up into the seal formation. Righthand side: -2300 m depth, in the middle of the reservoir.

A.1.2.4 Stress changes – More compliant seal and base

The poro-thermo-elastic stress changes have also been compared for heterogeneous elasticity, with seal and base formations having a 4x lower stiffness than the reservoir. Note that this is a significant contrast in stiffness, in reality it is likely less and differences resulting from heterogeneous elasticity are also less.

The comparison between SRIMA and DIANA FEA shows that, for a 4x more compliant seal and base formation (Figure 25, Figure 26, Figure 27):

- SRIMA overestimates the horizontal stress decrease in the cooled reservoir volume by ~25% (Figure 25, Figure 27)
- SRIMA overestimates the Coulomb stress increase within the cooled reservoir volume by ~25% and is thus conservative within the cooled reservoir volume.
- SRIMA underestimates the vertical stress increase by 50% and the horizontal stress decrease by <20% to the side of the cooled reservoir volume (left column Figure 27).
- SRIMA underestimates the Coulomb stress increase to the side of the cooled reservoir volume and is thus not conservative at this location. The difference is larger than for the uniform elasticity and 4x stiffer seal and base case, but <20%.

Again, the discrepancies are related to the use of analytical correlations to heterogeneous subsurface for which they were not developed

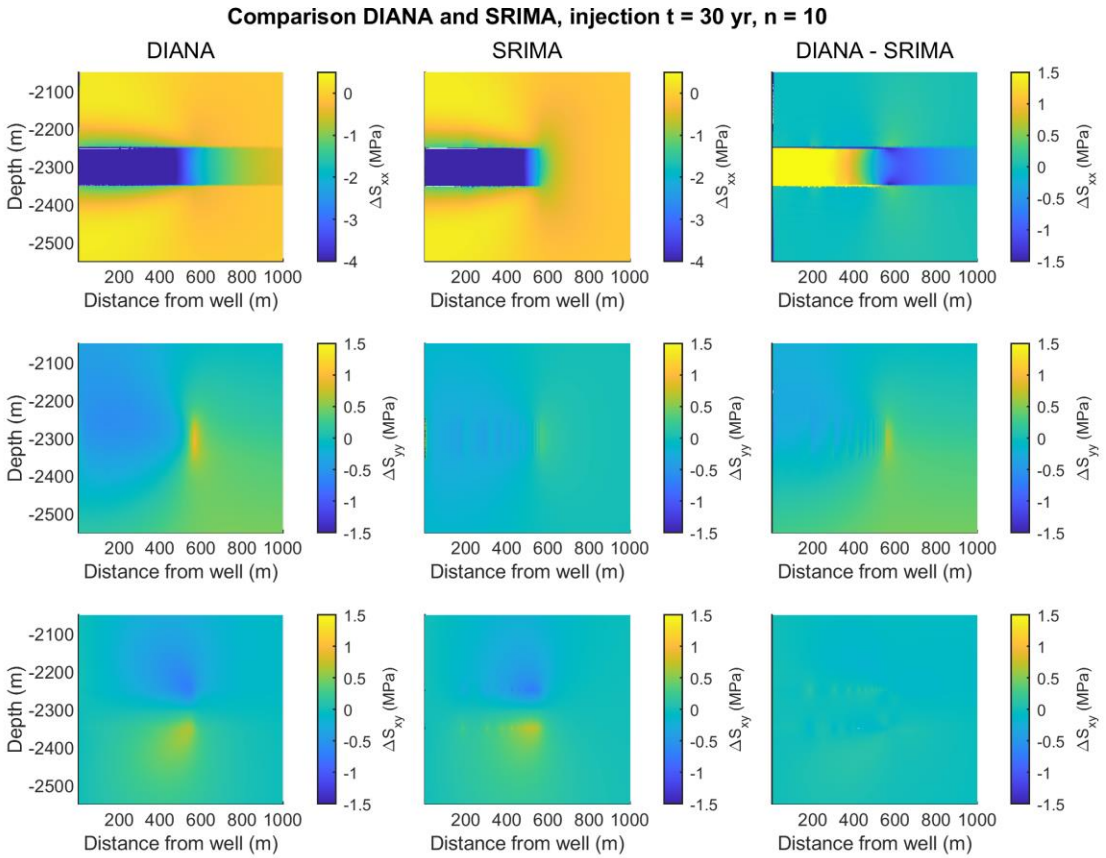

Figure 25 Stress changes modeled in DIANA and SRIMA and differences between stress changes in both models, for a 4x more compliant seal and base formation. Stress changes are computed after 30 years of injection. Horizontal stress change: ΔS_{xx}, vertical stress change: ΔS_{yy}, and shear stress change: ΔS_{xy}. Right column shows the difference in stress change between DIANA and SRIMA, with positive values indicating the stress computed in DIANA is larger than in SRIMA.

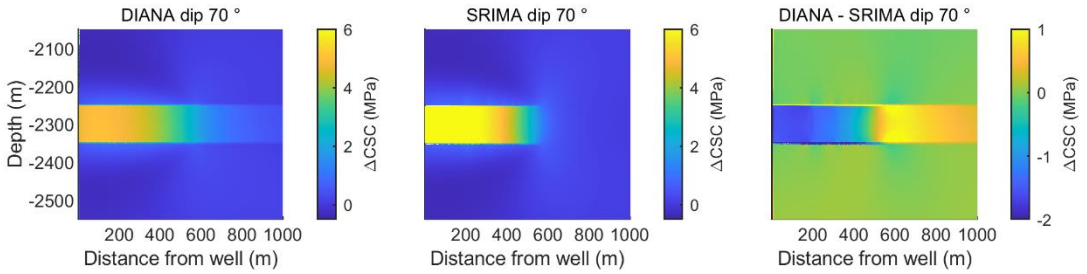

Figure 26 Coulomb stress changes modeled in DIANA and SRIMA and differences between stress changes in both models, for a 4x more compliant seal and base formation. Coulomb stress changes (ΔCSC) are computed after 30 years of injection, for a 70° dipping fault at all locations in the model domain. Right column shows the difference in stress change between DIANA and SRIMA, with positive values indicating the Coulomb stress computed in DIANA is larger than in SRIMA.

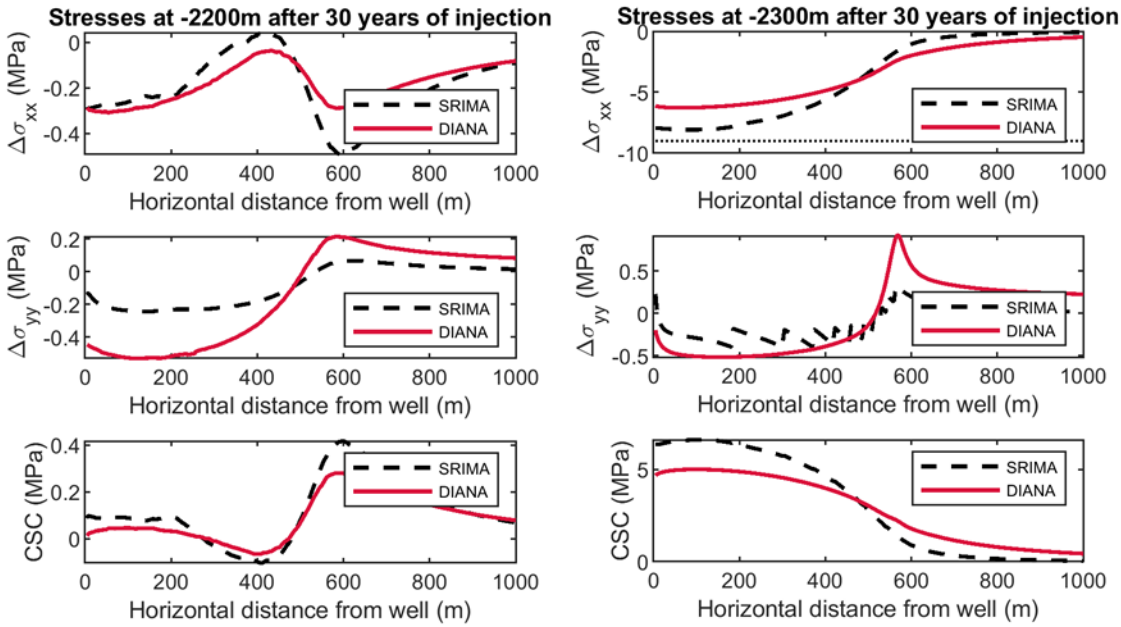

Figure 27 Comparison of horizontal and vertical stress changes and Coulomb Stress Changes computed in DIANA and SRIMA at different depths, for 4x more compliant seal and base formations. Lefthand side: -2200 m depth, 50 m up into the seal formation. Righthand side: -2300 m depth, in the middle of the reservoir.

A.1.2.5 Implications

For uniform elasticity, the agreement between DIANA and SRIMA is reasonably good (<7% difference in Coulomb Stress Change in most of the cooled volume), and, more importantly, SRIMA is conservative within the cooled volume. However, just outside the cooling front SRIMA is not conservative. This should be considered for fault reactivation studies. However, as the region where SRIMA is not conservative is limited in size, effects on magnitude calculation are expected to be very minor, as the magnitude depends on the logarithm of the affected fault area.

Compared to the uniform elasticity and the 4x stiffer seal and base, the 4 x more compliant seal and base scenario yields the biggest differences. However, in general the differences are either conservative or <20%, which, within the range of the overall parameter uncertainty and the logarithmic dependency of magnitude on slip zone area, is expected to have a minor result.

In general, a difference of factor 4 between reservoir stiffness and seal and base stiffness will not often occur. Mostly the mismatch will be smaller than in the examples presented.

A.1.3 Effect of fault offset on stress changes

The effect of reservoir offset along the (virtual) fault is ignored in SRIMA. However, in previous studies of induced stress changes it was shown that stress concentrations form on faults that offset depleting reservoir compartments (Mulders, 2003, Van den Bogert, 2015, Buijze et al., 2019, Jansen et al., 2019). These stress concentrations lead to a locally increased SCU and hence promote fault reactivation. In this section we analyze how ignoring fault offset in SRIMA

would affect the modelled SCU. We do this based on a comparison of SRIMA model simulations with a 2D plane-strain simulation where offset is accounted for: PANTHER (Physics-based semi(ANalytical) Tool for Human-induced Earthquake Rupture (https://github.com/TNO/PANTHER, v0.8).

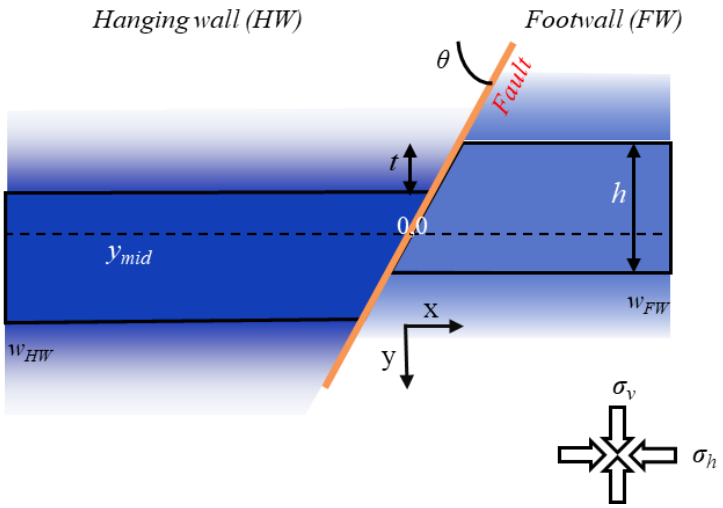

Figure 28 Plane-strain model geometry of PANTHER. There are two reservoir compartments cross-cut by a fault. Left side shows the hanging wall compartment (HW) with width w_{HW}, right side the footwall compartment (FW) with width w_{FW} offset reservoir compartments. H: thickness, t: throw, θ: dip, σ_v vertical stress, σ_h horizontal stress.

A.1.3.1 PANTHER model setup

PANTHER assumes a 2D plane-strain reservoir geometry (infinite extent in the out-of-plane dimension). Two reservoir compartments are offset by a fault. Reservoir compartments are prescribed a certain width (which can differ on either side of the fault) and height. For each timestep a uniform pressure and/or temperature change can be described to the reservoir compartments. This change can be independently varied with time and be different in either compartment or be zero in one of the compartments. Diffusion of pressure and temperature to the seal and base can be incorporated. Steady-state, vertical diffusion is assumed (equations 2 and 6). The resulting poro- and thermo-elastic stress changes are computed semi-analytically using the formulation by Jansen et al., 2019, adapted for thermo-elastic stress. Linear superposition of both effects is assumed – i.e., thermo-elastic strains have no effects on pore pressure. The stress changes are transformed to fault shear and effective normal stresses. These are added to the initial fault stresses, which are computed from the far-field stress gradients of σ_v, σ_{hmax} and σ_{hmin}, the pore pressure gradient, and the fault strike and dip.

Default input values of SRIMA v 1.0 were used in PANTHER (Table 4). Temperature and pressures at the fault location as computed in SRIMA were used in PANTHER, and the width of the footwall and hanging wall compartments was based on the extent of the cooled reservoir volume in SRIMA.

Table 4 Default input used for SRIMA (v.1.0 defaults) and PANTHER

Parameter	Value	Parameter	Value
Thickness (m)	100	$\Delta\sigma_v/\Delta y$ (MPa/km)	22
Mid depth (m)	-2050	$\Delta\sigma_{hmin}/\Delta y$ (MPa/km)	15.4
Dip (deg)	60 + varied	$\Delta\sigma_{hmax}/\Delta y$ (MPa/km)	15.4
Throw (m)	0 + varied	$\Delta P/\Delta y$ (MPa/km)	10.4
Young's modulus (Pa)	12e+9	Static friction coefficient (-)	0.6
Poisson's ratio(-)	0.25	Cohesion (MPa)	0
Biot's coefficient (-)	0.87	Thermal expansion coefficient (1/K)	1e-5
		Thermal diffusivity	1.5345e-6

A.1.3.2 Axisymmetric reservoir versus a plane-strain reservoir

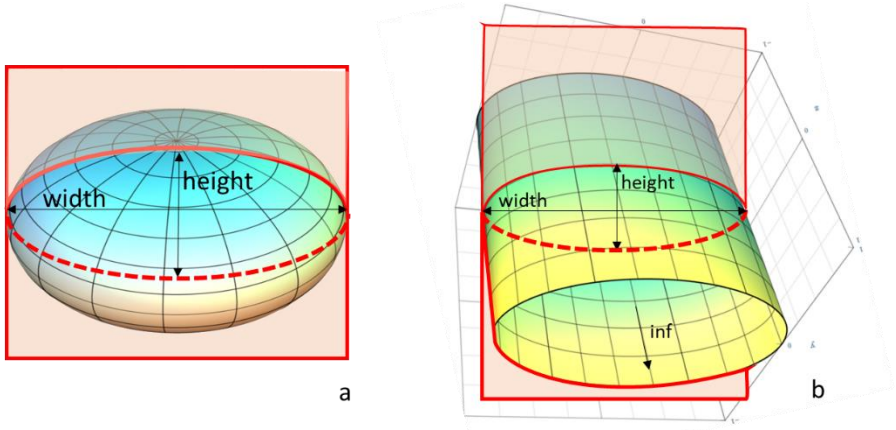

Figure 29 Two simplified end-member cases used to compare stress changes for a) an axi-symmetric geometry (oblate spheroid), and b) an elliptical cylinder which has a similar geometry in the in-plane section but of infinite length in the out-of-plane section (plane-strain).

The plane-strain geometry of PANTHER differs from the axisymmetric geometry employed in SRIMA. To warrant the comparison and to get a first-order insight into the differences between the two situations, the analytical solutions for stress changes in simplified geometries can be considered (Soltanzadeh & Hawkes, 2009). Analytical solutions for an axisymmetric geometry include those for an oblate spheroidal inclusion in a homogeneous elastic medium – i.e. a flattend elliptical disk (Figure 29a). For such an oblate spheroidal inclusion, the poro-elastic stress path parameters depend on aspect ratio – i.e., the height/thickness of cooled/pressurized volume – as shown in Figure 30a. A comparable geometry for a plane-strain setting is the elliptical cylinder, which in the in-plane section has the same geometry, but is of infinite length in the out-of-plane direction (Figure 29b). The elliptical cylinder results in the same γ_h and γ_v at aspect ratio's tending to zero. At higher aspect ratios the stress path parameters start to differ, up to 0.1 for aspect ratio's tending to 1 (i.e., height = thickness). The

difference between the axisymmetric solution and plane-strain solution affects mainly the normal stress change, since the normal stress is a function of both mean stress $(\sigma_h + \sigma_v)/2$, dip, and differential stress $(\sigma_v - \sigma_h)$, whereas the shear stress depends on the differential stress and dip only (Figure 30b). The difference between stress path parameters γ_v and γ_h for both geometries is not very different (curves have the same shape in Figure 30a), hence the effect on τ is limited. For the normal stress change the difference ranges from 0 at aspect ratio = 0, to 20% at aspect ratio = 1. If the width of the cooled/pressurized volume is at least 3x that of the height, the impact on normal stress should not be larger than 10%. An intuitive argument is found by the relatively large radius of the cooled zone in comparison with its thickness.

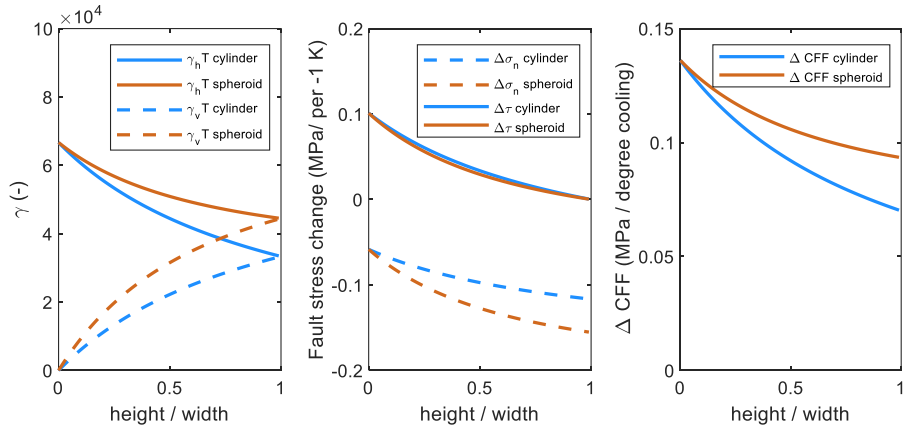

Figure 30 Difference in stress changes between and axisymmetric ellipsoid (oblate spheroid), and a plane-strain ellipsoidal cylinder. Left: stress path parameter γ (= $\Delta\sigma/\eta\Delta T$) for Poisson ratio 0.25, where η is the thermal expansion coefficient $1 \cdot 10^{-5}$. Center: induced stresses for 1 degree of cooling, on a fault dipping 60 degrees (in case of the elliptical cylinder, the strike is parallel to the long axis), and shear modulus 7 GPa. Right: resulting Coulomb Stress Change.

These ellipsoidal geometries give first order insights into the differences between plane-strain and axi-symmetric stress changes.

In the case of PANTHER and SRIMA the differences may be a bit different, as the temperature function in SRIMA is not uniform and the cooled reservoir volume does not have an elliptical shape. In particular towards the edges of the cooled volume some differences may arise, as contrary to the elliptical inclusions, stress changes throughout the pressurized or cooled volume are not uniform. Note also that the along-strike shear stress will be different in both cases, with the along-strike horizontal stress change being equal to the strike perpendicular horizontal stress change for the axisymmetric case, and (1 - 2ν) / (1 – ν) for the plane-strain case. Still for aspects ratios of the cooled volume of < 0.3 and at locations not too close to the edge the solutions are expected to be comparable.

A proper comparison can be made for zero-offset faults. Indeed, we found good agreement between SRIMA and PANTHER for the stresses on a fault through the reservoir that did not show an offset (Figure 31).

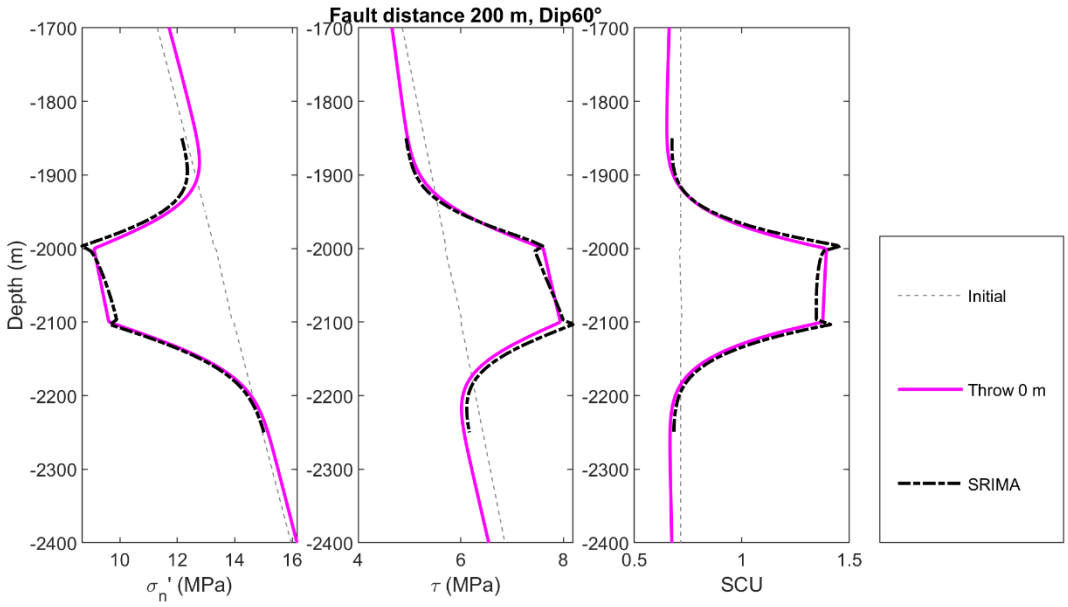

Figure 31 Comparison between PANTHER and SRIMA, for fault stress changes after 30 years of cooling. The fault location is taken 200 m from the injection well, the dip is set to 60 degrees. For PANTHER geometry a 0 m offset was imposed (violet line). Default SRIMA input parameters were used for both PANTHER and SRIMA.

A.1.3.3 A note on the effect of throw and the effect of P or T diffusion

Many prior works have analyzed the effect of offset on fault reactivation, in the framework of depleting gas fields (Mulders, 2003, Orlic et al., 2013, Van den Bogert, 2015, Buijze et al., 2019, Jansen et al., 2019). In these studies, a simplified pressure function was prescribed with a uniform pressure drop within the reservoir and no pressure change outside of the reservoir. The nature of the model geometry and this assumed pressure profile leads to positive and negative stress concentrations (singularities) in shear stress on the fault, at the top and base of the hanging wall and footwall compartments (Figure 32). These stress concentrations have often been used to explain enhanced fault stressing in depleting gas fields. However, these singularities are artificial, and the magnitude of the stress concentrations depends on the element size with which the singularity is resolved. Note that when elastic properties are different between the reservoir and base and cap rock, additional stress concentrations may develop. The combined effect of throw and variable elastic properties on the fault stresses needs to be evaluated in the future.

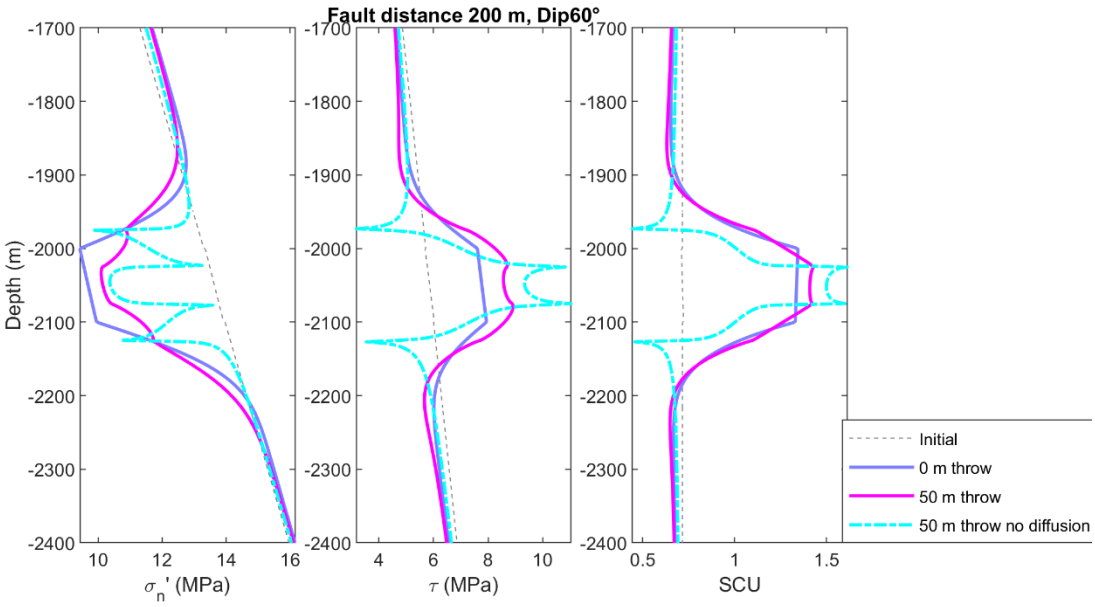

Figure 32 Effect of temperature diffusion on fault stresses. Fault stresses are computed after 30 years of production, on a fault 200 m away from the injection well, with a dip of 60°.

Accounting for temperature diffusion reduces the effect of reservoir offset on the fault stresses and SCU (Figure 32). The shear stress increase becomes less concentrated over the reservoir-reservoir juxtaposition and is smoothed out more towards the seal and base. The negative shear stress changes near the top and base of the reservoir interval disappear. Also, the normal stress distribution becomes less peaked, and the SCU is smoother. Also here, the negative SCU regions at the top and base disappear.
Hence, diffusion has a significant effect on the stress changes and should be considered. In the following sections the results of PANTHER are compared to SRIMA.

A.1.3.4 Comparison PANTHER & SRIMA: effect of throw

Figure 33 shows the fault stresses on a fault 200 m from the injection well with a dip of 60°. As shown earlier in A.1.3.2 the agreement between SRIMA and PANTHER for 0 m offset is good. For increasing throw both the effective normal stress and the shear stress in the reservoir become larger. The shear stress becomes more peaked, with a maximum in the reservoir center. In addition, the fault length over which the stress changes occur increases due to the offset reservoir geometry. The absolute differences in effective normal stress are up to 2-3 MPa, and 2 MPa for the shear stress. However, the effect on the SCU is minor, with SRIMA underestimating the SCU by <10% over <25% of the reservoir height.
Hence, in this situation the effect of throw on SCU, slipped area, and resulting magnitude will be minor, with SRIMA being conservative due to the larger fault area over which SCU >1.

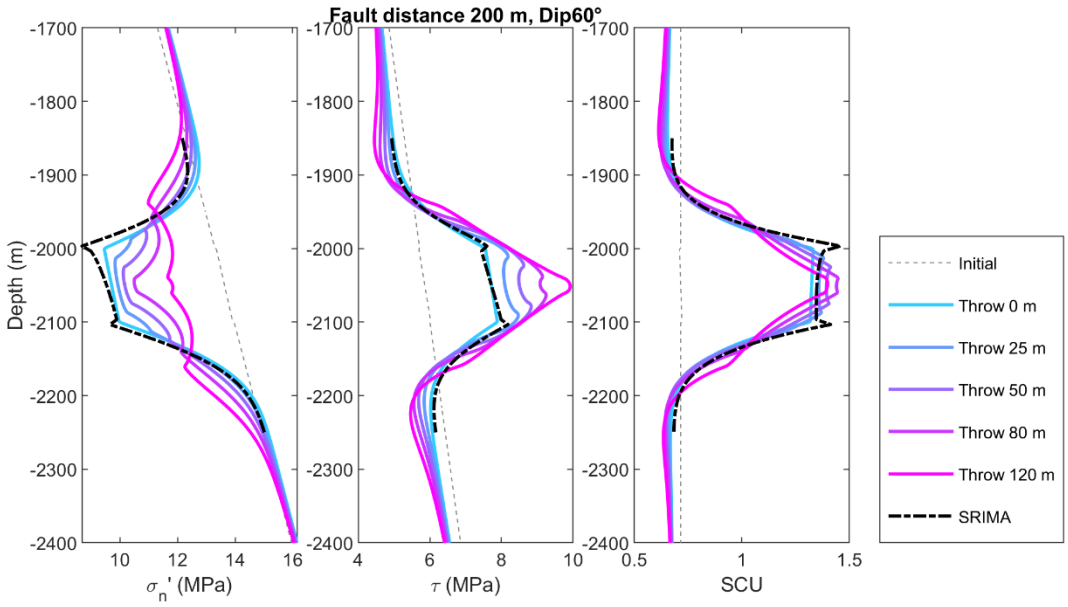

Figure 33 Comparison fault stresses computed in SRIMA and PANTHER. Fault stresses are computed after 30 years of production, on a fault 200 m away from the injection well, with a dip of 60°.

A.1.3.5 Combined effect of fault dip and throw

The relative change in effective normal stress and shear stress depends on the fault dip. For an optimal dip of 60° stress changes are most destabilizing. For steeper dips than 60°, the effective normal stress change increases and the shear stress change decreases, with the shear stress changes tending to 0 for 90° dip. This is visible in the SRIMA results of Figure 34 through Figure 36. For shallower dips the effective normal stress change becomes smaller (Figure 37, Figure 38).

Fault throw however concentrates the shear stresses towards the center of the reservoir formations, and results in lower effective normal stress changes. With increasing dip, the mismatch between fault stresses in the 0 m throw case and other throw scenario's increases. The larger the throw, the larger the mismatch.

In terms of SCU: with increasing dip SRIMA results increasingly underestimate the SCU. This is most clearly visible in the 90° dip scenario, where a 0 m throw case does not result in shear stress changes, whereas fault throw does lead to shear stress changes of up to 2.5 MPa (Figure 36). Note that overall, this is a relatively stable scenario as initial shear stress in such a case would be 0 MPa. However, it is a scenario where SRIMA is not conservative. For a dip of 70° the mismatch in SCU is 0.1 – 0.2, or < 20% of the SCU change depending on the throw. For a throw less than 0.5 of the reservoir height (here < 50 m) the mismatch between the maximum SCU is < 15%. However, the fault length where SCU > 1 is the same for SRIMA and the scenarios with a non-zero throw, and in this case the effect on slip area and magnitude would be very small. However, the time to first reactivation would be smaller for the non-zero throw compared to the zero-throw scenario, since the non-zero throw SCU is peaked. There would thus be a certain time window where the zero-throw scenario would underestimate the slip zone area.

For shallower dips than 60° SRIMA remains conservative (Figure 37, Figure 38).

Based on these findings, it is recommended to use SRIMA for fault geometries with dips of 60° and with throws is less than 0.5 the reservoir height

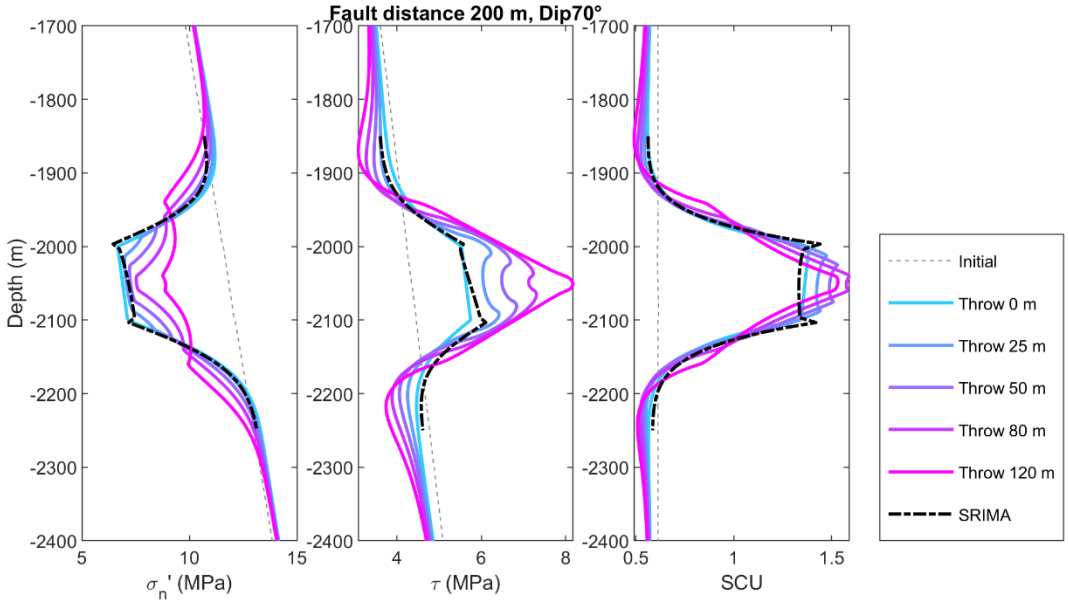

Figure 34 Comparison fault stresses computed in SRIMA and PANTHER. Fault stresses are computed after 30 years of production, on a fault 200 m away from the injection well, with a dip of 70°.

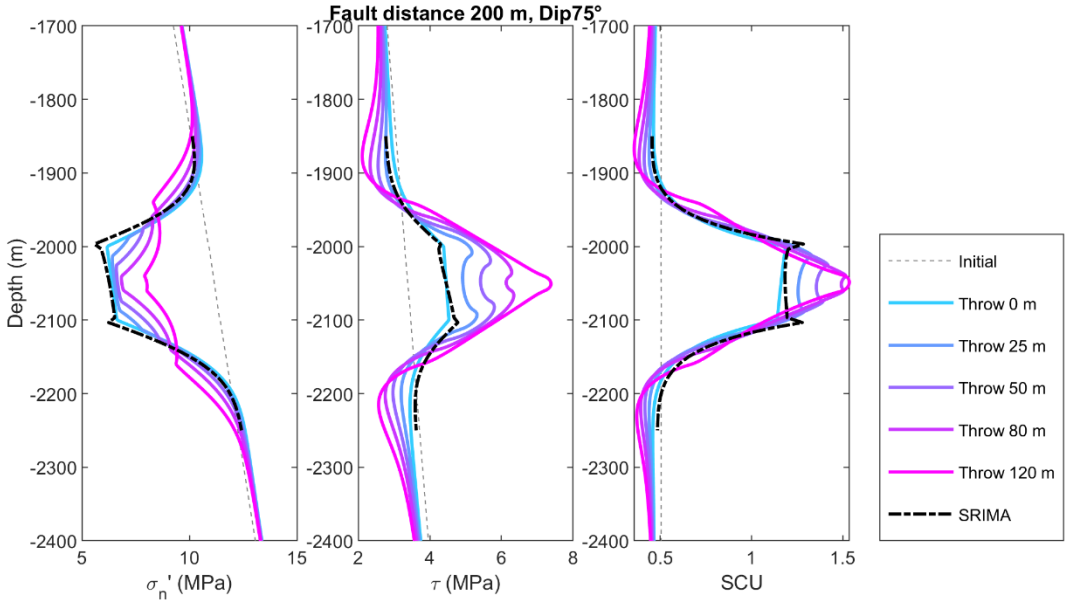

Figure 35 Comparison fault stresses computed in SRIMA and PANTHER. Fault stresses are computed after 30 years of production, on a fault 200 m away from the injection well, with a dip of 75°.

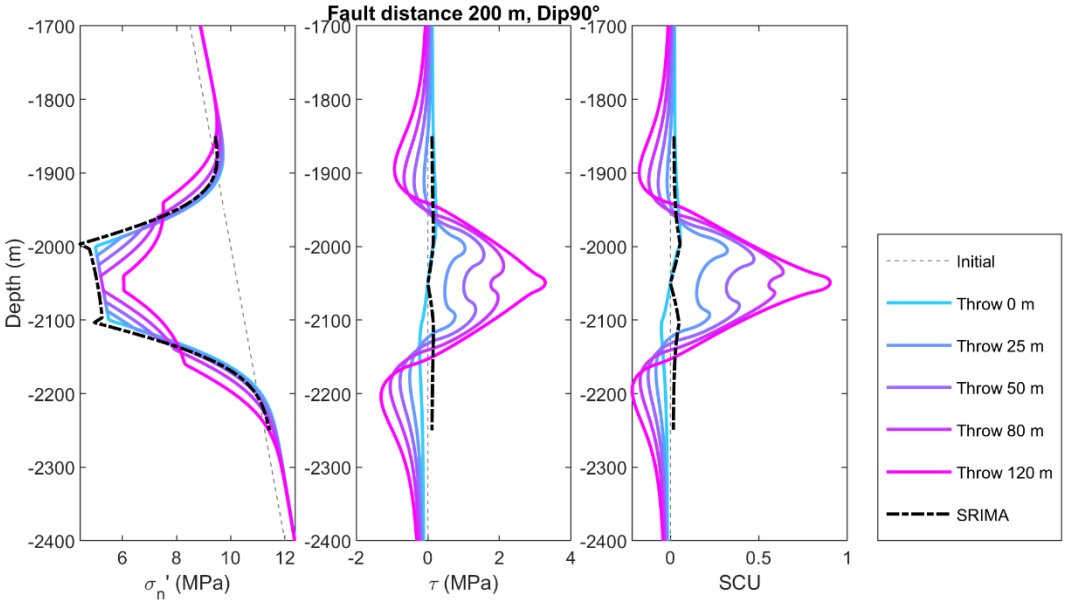

Figure 36 Comparison fault stresses computed in SRIMA and PANTHER. Fault stresses are computed after 30 years of production, on a fault 200 m away from the injection well, with a dip of 90°.

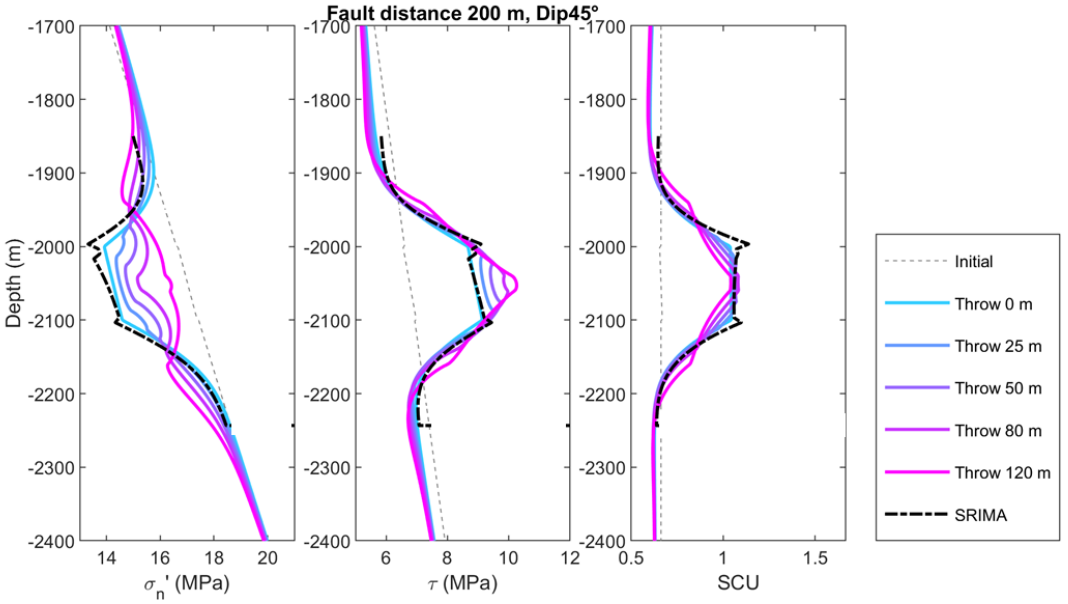

Figure 37 Comparison fault stresses computed in SRIMA and PANTHER. Fault stresses are computed after 30 years of production, on a fault 200 m away from the injection well, with a dip of 45°.

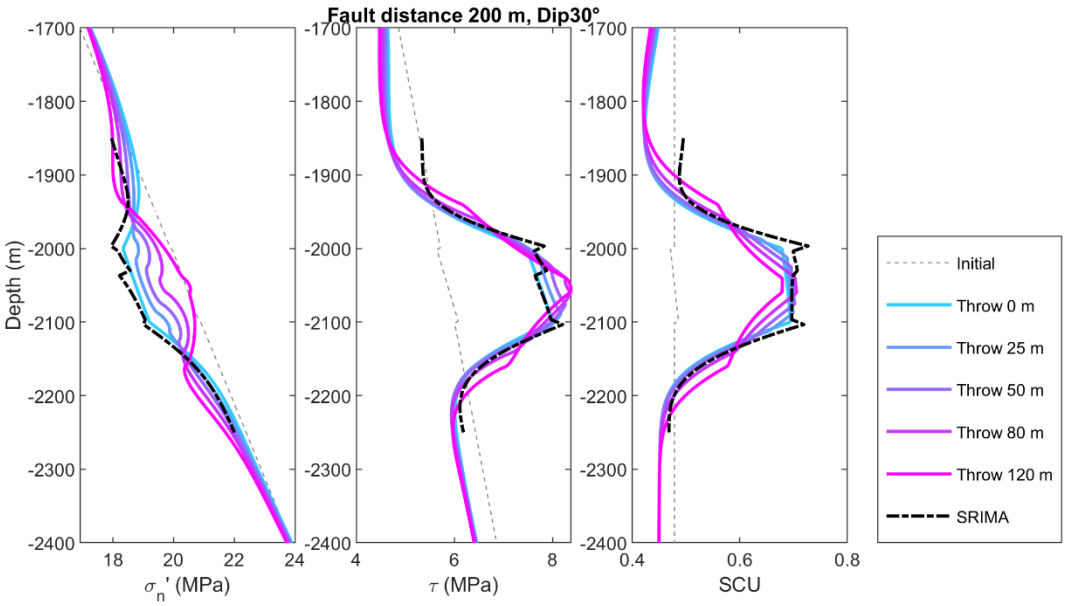

Figure 38 Comparison fault stresses computed in SRIMA and PANTHER. Fault stresses are computed after 30 years of production, on a fault 200 m away from the injection well, with a dip of 30°.

A.1.3.6 Bounding or sealing faults

For fault throws larger than the reservoir thickness or for low-permeable fault zone material, faults could be sealing. Sealing faults cannot be simulated in SRIMA, but in PANTHER the temperature change in the e.g., the footwall compartment can be set to zero (Figure 39). In such a case, the change in SCU is much less compared to non-sealing or non-bounding faults. Hence, SRIMA is conservative with respect to sealing or bounding fault scenario, as long as the fault dip is < 70°.

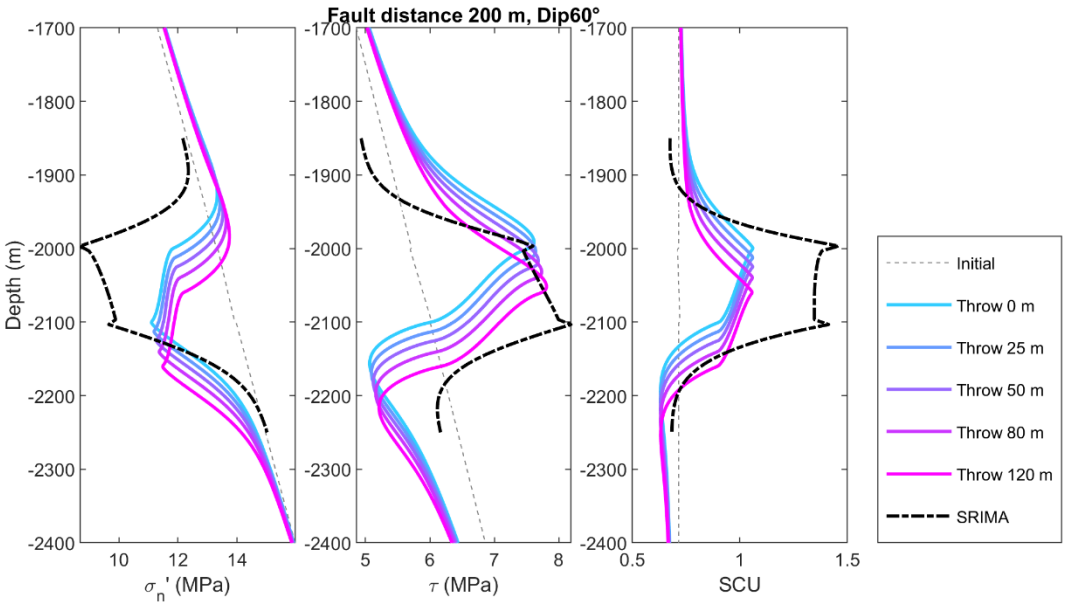

Figure 39 Comparison fault stresses computed in SRIMA and PANTHER, for a sealing fault scenario. Fault stresses are computed after 30 years of production, on a fault 200 m away from the injection well, with a dip of 60°. Temperature change in the footwall compartment is set to 0.

A.1.3.7 Implications

Based on the comparison between SRIMA and PANTHER, it is recommended to apply SRIMA for cases where the reservoir throw is <0.5 that of the reservoir and the dip is <70°. If the throw is tending towards 0, allowable dips can be larger. For sealing / bounding faults, SRIMA gives a much more conservative estimate of fault stress change than expected for sealing / bounding faults. It is recommended in the future to further assess the effect of throw using both 2D and 3D solutions (e.g. obtained from Finite Element modeling) for a wide variety of throws, dips, elastic properties, and elasticity contrasts.